Earth and Planetary Science Letters 435 (2016) 147–158

Contents lists available at ScienceDirect

Earth and Planetary Science Letters

www.elsevier.com/locate/epsl

Lithospheric rheology constrained from twenty-five years of postseismic deformation following the 1989 M_w 6.9 Loma Prieta earthquake

Mong-Han Huang [a,b,c,*], Roland Bürgmann [a,b], Fred Pollitz [d]

[a] Department of Earth and Planetary Science, University of California, Berkeley, CA 94720-4767, USA
[b] Berkeley Seismological Laboratory, University of California, Berkeley, CA 94720-4767, USA
[c] Jet Propulsion Laboratory, California Institute of Technology, 4800 Oak Grove Drive, Pasadena, CA 91109, USA
[d] U.S. Geological Survey, 345 Menlo Park, CA 94025, USA

ARTICLE INFO

Article history:
Received 23 July 2015
Received in revised form 4 December 2015
Accepted 17 December 2015
Available online xxxx
Editor: P. Shearer

Keywords:
Loma Prieta earthquake
postseismic displacement
lithospheric rheology
viscoelastic relaxation
San Francisco Bay Area

ABSTRACT

The October 17, 1989 M_w 6.9 Loma Prieta earthquake provides the first opportunity of probing the crustal and upper mantle rheology in the San Francisco Bay Area since the 1906 M_w 7.9 San Francisco earthquake. Here we use geodetic observations including GPS and InSAR to characterize the Loma Prieta earthquake postseismic displacements from 1989 to 2013. Pre-earthquake deformation rates are constrained by nearly 20 yr of USGS trilateration measurements and removed from the postseismic measurements prior to the analysis. We observe GPS horizontal displacements at mean rates of 1–4 mm/yr toward Loma Prieta Mountain until 2000, and ∼2 mm/yr surface subsidence of the northern Santa Cruz Mountains between 1992 and 2002 shown by InSAR, which is not associated with the seasonal and longer-term hydrological deformation in the adjoining Santa Clara Valley. Previous work indicates afterslip dominated in the early (1989–1994) postseismic period, so we focus on modeling the postseismic viscoelastic relaxation constrained by the geodetic observations after 1994. The best fitting model shows an elastic 19-km-thick upper crust above an 11-km-thick viscoelastic lower crust with viscosity of $\sim 6 \times 10^{18}$ Pa s, underlain by a viscous upper mantle with viscosity between 3×10^{18} and 2×10^{19} Pa s. The millimeter-scale postseismic deformation does not resolve the viscosity in the different layers very well, and the lower-crustal relaxation may be localized in a narrow shear zone. However, the inferred lithospheric rheology is consistent with previous estimates based on post-1906 San Francisco earthquake measurements along the San Andreas fault system. The viscoelastic relaxation may also contribute to the enduring increase of aseismic slip and repeating earthquake activity on the San Andreas fault near San Juan Bautista, which continued for at least a decade after the Loma Prieta event.

1. Introduction

Periods of accelerated postseismic deformation following large earthquakes reflect the response of the Earth's lithosphere to sudden coseismic stress changes. Thus, detailed geodetic measurements of postseismic relaxation effectively probe the rheology of rocks and faults at depth (Bürgmann and Dresen, 2008). Transient post-earthquake relaxation includes contributions from (1) fault afterslip above (Bürgmann et al., 1997; Johnson et al., 2006; Freed and Bürgmann, 2004) and below (Tse and Rice, 1986) the base of the seismogenic zone, (2) viscous flow in the lower crust and upper mantle (Bürgmann and Dresen, 2008; Thatcher and Pollitz, 2008), (3) poroelastic rebound in the upper crust due to fluid flow in response to coseismic pressure changes (Jónsson et al., 2003; Peltzer et al., 1996), and (4) recovery of coseismic dilatancy by fault-zone compaction (Savage et al., 1994; Savage and Svarc, 2010; Fielding et al., 2009). For relatively small earthquakes, shallow and rapidly decaying afterslip and poroelastic relaxation dominate the observed postseismic transients and contributions from below the seismogenic zone are difficult to resolve (Jónsson et al., 2003; Pollitz et al., 1998). Depending on the magnitude of the earthquake and the viscosity structure of the lithosphere, viscous relaxation

* Corresponding author at: Jet Propulsion Laboratory, California Institute of Technology, 4800 Oak Grove Drive, Pasadena, CA 91109, USA. Tel.: +1 818 354 4456.
E-mail address: mong@seismo.berkeley.edu (M.-H. Huang).

http://dx.doi.org/10.1016/j.epsl.2015.12.018
0012-821X/© 2015 Published by Elsevier B.V.

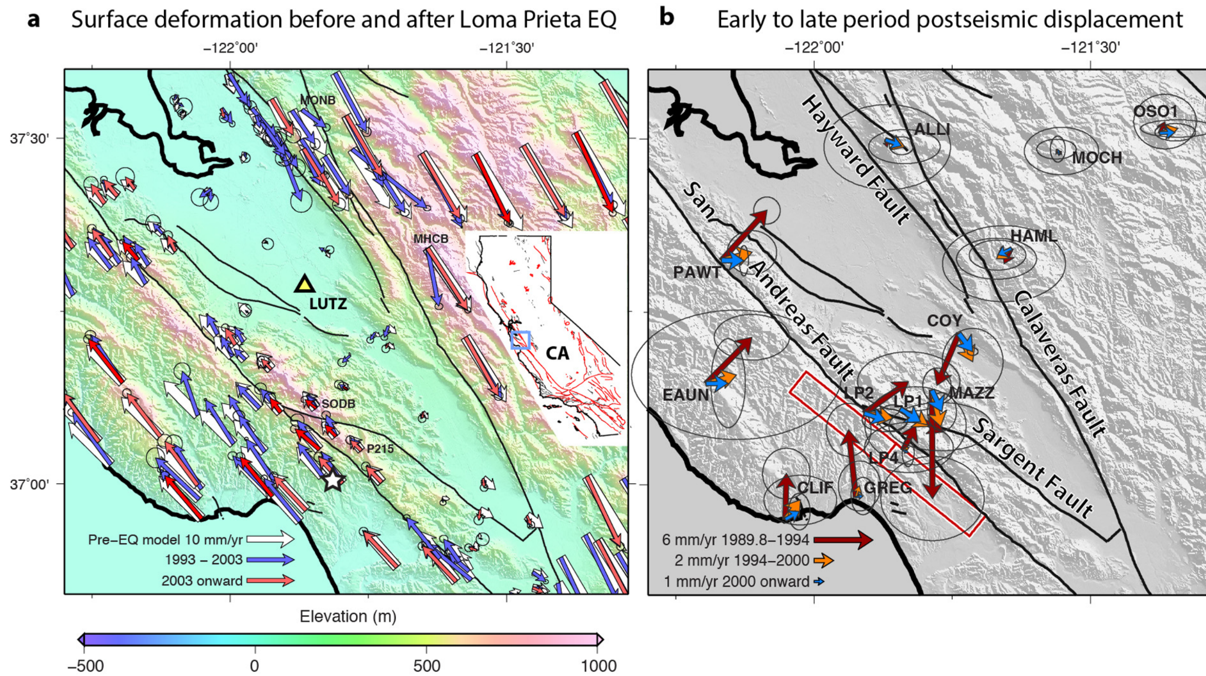

Fig. 1. Geodetic horizontal measurements in the southern San Francisco Bay Area, shown in the blue box in the map. (a) Surface deformation before and after the Loma Prieta earthquake relative to station LUTZ (yellow triangle). The white arrows are the preseismic secular motion prediction inverted from EDM measurements (Bürgmann, 1997); the blue arrows are the BAVU GPS measurements during 1993–2003 (d'Alessio et al., 2005); the red arrows are the USGS velocities from campaign and continuous GPS measurements since 2003. The white star indicates the Loma Prieta earthquake epicenter. (b) The Loma Prieta postseismic displacements during 1989–1994, 1994–2000, and 2000–present. The circles are the standard deviation of the logarithmic fitting [Eq. (1)] misfit to each GPS station in each time period. The GPS time series is shown in Fig. S2a. Secular motions have been removed based on Bürgmann (1997), and the postseismic displacement is relative to MOCH. The black lines are the major fault lines, and the red lines are the coseismic fault geometry by Marshall et al. (1991). (For interpretation of the references to color in this figure legend, the reader is referred to the web version of this article.)

at depth dominates transient deformation, especially at larger distances from the coseismic rupture (Freed et al., 2012).

Much of our knowledge of the earthquake cycle and the rheology of the deep San Andreas fault (SAF) system in central California is based on interpretation of geodetic measurements collected in the decades following the 1906 San Francisco earthquake that ruptured a ∼400-km-long section of the SAF (Kenner and Segall, 2003). Kenner and Segall (2003) consider data collected between 1906 and 1995 in a systematic evaluation of various first-order models of lower-crustal and upper-mantle structure and rheology. They find that models incorporating vertical viscous shear zones in the lower crust within an otherwise elastic or viscous layer provide a good fit to the geodetic data, and are consistent with seismic studies that suggest that narrow fault zones extend through the entire crust (Henstock et al., 1997). The occurrence of the M_W 6.9 Loma Prieta earthquake provides the first opportunity since 1906 to study postseismic relaxation. Our work here presents the first attempt of measuring over 20 yr of Loma Prieta postseismic deformation with modern space geodetic tools to estimate rheological parameters in the region.

The deformation measured with GPS immediately following the Loma Prieta earthquake revealed significant postseismic contraction and right-lateral shear across the southern Santa Cruz Mountains northeast of the SAF (Savage et al., 1994; Bürgmann et al., 1997). The localized nature of the transient displacement field indicates relatively shallow deformation sources. The measurements of the first five years can be interpreted to be due to aseismic right-oblique fault slip on or near the coseismic rupture, as well as thrusting up-dip of the buried rupture within the Foothills thrust belt (Bürgmann et al., 1997). Analysis of the time-varying nature of the deformation signal suggests that the shallow transient thrusting ceased in 1992 while resolvable oblique shear at seismogenic depths may have persisted through 1994 (Segall et al., 2000). Alternatively, afterslip on the downdip extension of the coseismic rupture plus a fault-normal collapse of the rupture zone can explain the observed surface motions (Savage and Svarc, 2010). Analysis of the GPS measurements did not resolve a significant contribution of lower crustal or upper mantle relaxation processes, during the first five years following the event (Pollitz et al., 1998).

Since the Loma Prieta earthquake, several studies have focused on the interseismic deformation in the Bay Area that accommodates the secular motion between the North American plate and the Pacific plate. d'Alessio et al. (2005), Johanson and Bürgmann (2005), Bürgmann et al. (2006), and Johnson and Fukuda (2010) estimate Bay Area interseismic deformation models based on campaign and continuous GPS measurements after 1994 (Fig. 1a). Although the model-predicted displacements generally agree with most of the GPS measurements, a systematic model misfit exists near the Loma Prieta earthquake area in these studies (Fig. S1). This result indicates a mechanism that cannot be predicted by steady interseismic strain accumulation across the regional fault system. In addition, Bürgmann et al. (2006) found a model residual indicating subsidence along the restraining bend of the SAF in which the Loma Prieta earthquake occurred in their joint analysis of the horizontal GPS velocity field and Persistent Scatterer Interferometric Synthetic Aperture Radar (PSInSAR) data.

In this study, we argue that this systematic residual is due to viscoelastic relaxation (VER) of the lower crust and upper mantle following the Loma Prieta earthquake, a process that is still acting in this area after 1994. The pre-Loma Prieta interseismic deformation is estimated using precise trilateration measurements collected since the early 1970s (Lisowski et al., 1991). To obtain a ∼25-yr-long post-Loma Prieta observation, we combine campaign and continuous GPS measurements collected during 1989.8–2014 (Segall et al., 2000; USGS, 2015). We also generate an 18-yr-long InSAR time series between 1992 and 2010 with data from both the ERS-1/2 and Envisat satellites. We use these geodetic data to determine contributions from both afterslip and VER to the tran-

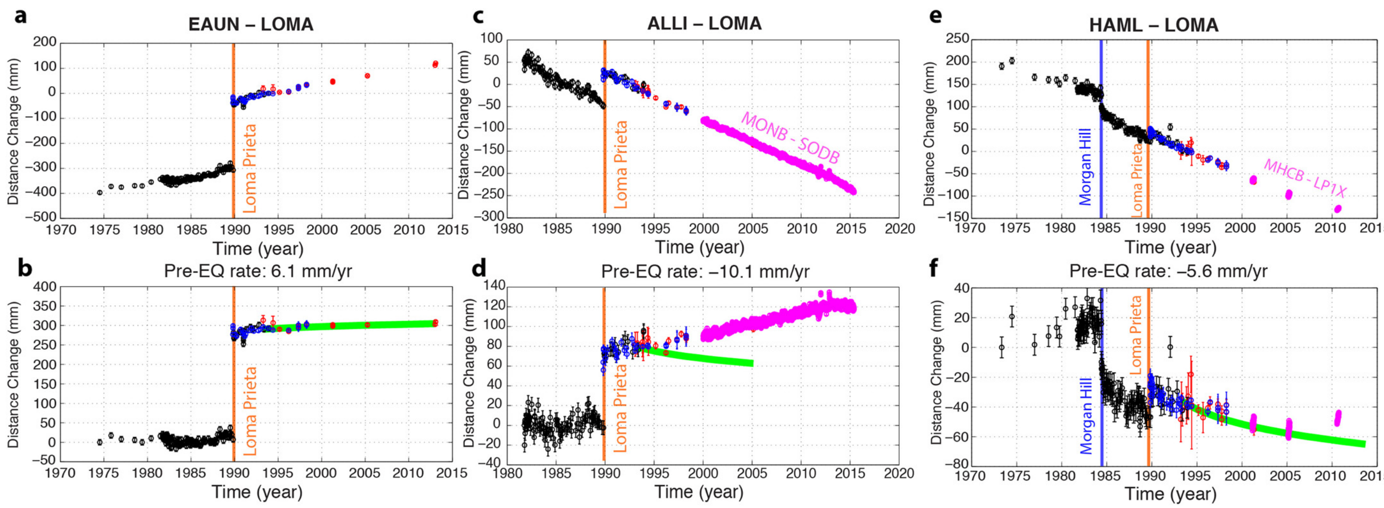

Fig. 2. Distance changes between selected stations before and after the Loma Prieta earthquake (see Fig. 1b for the location of stations). (a) Lengthening between stations EAUN and LOMA (or LP1) and after removing interseismic secular motion (b). The secular motion in (b) is removed based on Bürgmann et al. (1997). (c–d) ALLI–LOMA, and (e–f) HAML–LOMA. The green line in each sub-figure shows the predicted shortening due to viscoelastic relaxation based on the best-fitting model (Fig. 5a). The magenta points are distance change between BARD sites MONB–SODB (c and d) or MHCB–SODB (e–f), where MONB is close to ALLI, MHCB is close to HAML, and SODB is 10 km northwest of LOMA. Locations of all substitute stations are shown in Fig. 1a. (For interpretation of the references to color in this figure legend, the reader is referred to the web version of this article.)

sient deformation and estimate viscosities in the lower crust and uppermost mantle of the Bay Area.

2. Geodetic data

The U.S. Geological Survey (USGS) surveyed trilateration networks in the San Francisco Bay area, from 1973 (Lisowski et al., 1991) until as late as three years after the Loma Prieta event. Electronic Distance Measurement (EDM) observations detect changes in distance between station pairs that have been used to determine the secular velocity field between the North American Plate and the Pacific Plate (Lisowski et al., 1991). Bürgmann (1997) used the trilateration data to solve for the horizontal interseismic velocity field in the southern San Francisco Bay Area and developed a dislocation model inverted from the trilateration line-length change rates. This model is composed of 78 individual fault segments, and each fault segment has a uniform-slip dislocation in an elastic, homogeneous, and isotropic half-space. We adopt the same fault dislocations and slip rates to forward model the interseismic velocity before the Loma Prieta earthquake for each GPS station (white arrows in Fig. 1a).

Segall et al. (2000) analyzed daily GPS solutions at 62 stations collected from 1989.8 to 1998.3 (red dots in Fig. S2), and used a Network Inversion Filter to model time-dependent afterslip of the Loma Prieta earthquake. They modeled relative baseline vectors by subtracting the position of a frequently observed reference site (LP1 on Loma Prieta Mountain) from the other simultaneously observed positions, in order to minimize the errors in the absolute position determinations due to translational biases in the reference frame. Later on, d'Alessio et al. (2005) published the Bay Area velocity unification (BAVU) solutions based on more than 200 campaign and continuous GPS measurements collected between 1993 and 2003 (Fig. 1a; http://seismo.berkeley.edu/~burgmann/RESEARCH/BAVU/). Most of the GPS stations used in Segall et al. (2000) continued to be surveyed for BAVU (Fig. 1a). In addition, the USGS (Savage and Svarc, 2010) also resurveyed many of the GPS stations through early 2013 (http://earthquake.usgs.gov/monitoring/gps/SFBayArea_SGPS/). Data from the Bay Area Regional Deformation (BARD) and Plate Boundary Observatory (PBO) continuous GPS networks complement the campaign measurements (http://earthquake.usgs.gov/monitoring/gps/SFBayArea/). To generate a continuous postseismic displacement time series, we combine GPS measurements from Segall et al. (2000), BAVU (d'Alessio et al., 2005), the USGS campaign survey data, and the BARD and PBO observations (see Section 3.2 for more detail). The main challenge of combining the different GPS data sets lies in their heterogeneous observation periods and variable uncertainties. In addition, it is increasingly difficult to separate the interseismic secular motion from later-stage post earthquake measurements.

We use 53 European Space Agency (ESA) ERS-1/2 SAR descending acquisitions (Track: 70) between 1992 and 2006 and 46 Envisat ASAR descending acquisitions (Track: 70) between 2005 and 2010 (see Tables S1 and S2 for all acquisitions). All interferograms are generated using ROI_PAC 3.0 (Rosen et al., 2004), and we use the 90 m Shuttle Radar Topography Mission (SRTM) Digital Elevation Model (DEM) to correct the phase due to topography. Snaphu 1.4.2 (Chen and Zebker, 2002) is used for the phase unwrapping. We use a small baseline subset (SBAS, Berardino et al., 2002) method to generate time series of stable surface point scatterers. We generate interferograms that have less than 250 m perpendicular orbit separation and three years temporal baselines, respectively. We consider a point scatterer to be stable if the phase measurement at that point maintains its spatial correlation higher than 0.4 in at least 50% of all interferograms. We processed 392 interferograms (Fig. S3) from the 99 acquisitions, so solving the time series turns out to be an over-determined inverse problem (Huang et al., 2014).

3. Postseismic deformation

3.1. Pre- and postseismic baseline-length measurements

We combine the 1970–1990 EDM data (Lisowski et al., 1991), 1989.8–1998 campaign GPS measurements (Segall et al., 2000), and 1993–2014 USGS campaign and PBO continuous GPS (CGPS) data to estimate the pre-, co-, and postseismic distance changes between station pairs EAUN–LOMA, ALLI–LOMA, and HAML–LOMA (see Fig. 1 for station locations). The distance change is a projection of horizontal displacement between two stations onto the azimuth between stations. Figs. 2a, c & e show the line-length changes of different station pairs where black, blue, red, and pink points represent the EDM, 1989.8–1998 GPS, 1993–2014 campaign GPS, and post-2000 CGPS data, respectively. We use the interseismic model proposed by Bürgmann (1997) (white arrows in Fig. 1a) to remove secular motion contribution from the post-earthquake distance change measurements (Figs. 2b, d & f). For station pair EAUN–LOMA, the preseismic lengthening rate is 6.1 mm/yr (positive indicates lengthening), and the postseismic rate falls back to the preseismic rate after 2000 (<1 mm/yr; see Fig. 2b). For station pair ALLI–LOMA, the preseismic shortening rate is −10.1 mm/yr and stable postseismic shortening rate until 2012 (Fig. 2d). Note that we extend the time series by adopting nearby CGPS stations MONB and SODB to replace ALLI and LOMA after 2000. A similar approach is used for pair HAML (MHCB)–LOMA (LP1) (Fig. 2e). In this pair, there is an additional distance change in 1984 due to the *M* 6.2 Morgan Hill earthquake on the Calaveras fault. The postseismic transient of this event also affected the shortening rate prior to the 1989 Loma Prieta event. In fact, the Loma Prieta earthquake contributed less coseismic shortening of this baseline than the Morgan Hill earthquake. After removing secular motion, there is still ∼2 mm/yr shortening rate residual before the Morgan Hill event (Fig. 2f). Due to fewer measurements on LP1X, we choose nearby CGPS stations SODB and P215, both about 9 km far away from LOMA for this comparison (Figs. S3a–b). We further examine the distance changes between HAML, LOMA, and AMER in Supplementary Information S1 to explore Morgan Hill earthquake related displacement between these stations. The station AMER is west of the Calaveras fault, and the BARD GPS station LUTZ was built near AMER and surveyed continuously since 1996 (Fig. 1a).

3.2. Postseismic GPS displacement time series

To estimate the GPS time series since the Loma Prieta earthquake, we focus on benchmarks surveyed by Segall et al. (2000) and USGS (2015). The uncertainty of GPS positions relative to LP1 is 3–6 mm for the Segall et al. (2000) dataset, and ∼3 mm for the *USGS* dataset based on uncertainty estimations in their solutions. Due to higher GPS positioning uncertainty prior to 1995, we calculate site displacements at each epoch relative to station LP1 (also known as LP1X or LOMA) (Segall et al., 2000). We choose LP1 because it is densely surveyed during the 1989 and 2010 time period (Fig. S2a). We do not reprocess the GPS data, and we assume 1994 as the reference time because all GPS data sets include common measurements between 1994 and 1995. As a result, we are able to combine the solutions in a consistent local framework. We use the Bürgmann (1997) model to estimate and remove the interseismic contribution to the station displacements. We use logarithmic fits to the east and north components of the postseismic-only time series at each GPS station with a logarithmic function:

$$D(t) = D_{x,y} \ln(1 + t/\tau), \tag{1}$$

where $D_{x,y}$ contains the estimated postseismic amplitudes of the east and north displacement components. The logarithmic relaxation time (τ) describes the decay of postseismic displacement, and t is the observation time of each GPS record since the initiation of the postseismic period. For each station, we vary both $D_{x,y}$ and τ until obtaining a minimum model misfit of each component in the time series. Fig. S2a shows the combined time series of the east and north components and the corresponding best-fitting logarithmic functions. However, this LP1 referenced framework cannot well characterize postseismic displacement as LP1 is close to the epicenter and has significant postseismic displacement. As a result, we choose a stable far-field station MOCH east of the Calaveras fault as the reference station for postseismic displacement.

We refer to 1989–1994 as “early” and 1994 onwards as “late” periods of the Loma Prieta postseismic deformation in part because of the apparent change of dominating mechanism (Segall et al., 2000). We plot the estimated early-to-late period postseismic displacements of each GPS station in Fig. 1b based on their best-fitting $D_{x,y}$ and τ values. The red, orange, and blue arrows are total postseismic displacements in 1989–1994, 1994–2000, and 2000–2013, respectively. We separate three time periods in order to highlight the afterslip dominated period (1989–1994; Segall et al., 2000) and the decay of postseismic relaxation since 1994. Similar to the early postseismic period, the more recent displacements also show NE–SW convergence with a strike–slip component, but the amplitude is about three times lower than in the early period. Across the southern Santa Cruz Mountains, southwest of the Foothills thrust belt, all GPS measurements show a convergent motion with a right-lateral strike–slip component. The velocities of stations around the Foothills thrust belt are generally less than 3 mm/yr since 1994. Since 2003, GPS and CGPS measurements (red arrows in Fig. 1a) show displacements very similar to the pre-Loma Prieta period (white arrows in Fig. 1a).

3.3. 1992–2010 InSAR measurements

InSAR observations complement the GPS measurements and are particularly sensitive to vertical motions. Fig. 3 shows the InSAR Line-of-sight (LOS) velocity in the Loma Prieta area relative to a reference pixel at the continuous GPS station LUTZ during 1992–2000 (Fig. 3a) and 2000–2010 (Fig. 3b), respectively. Note the InSAR reference point is different from GPS because point scatterers east of the Calaveras fault are less reliable due to higher vegetation density (Fig. S4). LUTZ is located on bedrock and is less sensitive to hydrologic related seasonal surface deformation (Chaussard et al., 2014). We remove the secular motion contribution using the same Bürgmann (1997) interseismic model in order to highlight postseismic deformation. We also include the vertical secular motion contribution because the LOS direction is a projection of 3D motions into the 1D LOS direction. The LOS velocity map spanning a larger region can be found in Fig. S4, and positive LOS-change values represent range decrease. The full-size interferogram (Fig. S4) shows substantial uplift and subsidence in the Santa Clara Valley that is associated with seasonal and longer-term groundwater-level changes in the underlying aquifer (Schmidt and Bürgmann, 2003; Chaussard et al., 2014). Supplementary Information S2 provides more detail about the surface deformation in this area, and Supplementary Information S3 describes how seasonal variation in the InSAR time series is estimated and removed from the time series.

South of the Santa Clara Valley near Almaden and Morgan Hill (Fig. 3), there is a change of LOS velocity between the two periods. In 1992–2000 (Fig. 3a), a uniform InSAR range increase (blue) is obtained in the hilly area, consistent with surface subsidence of up to ∼2 mm/yr. In the 2000–2010 period, this deformation pattern is not found (Fig. 3b). Time series of three points taken in the Almaden–Morgan Hill area (Fig. 4) further illustrate the change of LOS displacement with time. Generally there is a decay of LOS rates to insignificant motions from 1992 to 2000 (Fig. 4a–b), but in the south (Fig. 4c) no significant changes in rate can be resolved. Even though there are no well-correlated InSAR points closer to Loma Prieta, we infer the apparent subsidence south of the Santa Clara Valley in 1992–2000 to be associated with the Loma Prieta postseismic deformation. The maximum subsidence rate in this region is ∼2 mm/yr in 1992–2000, and the subsiding area is consistent with the pattern seen in independently processed data in Bürgmann et al. (2006) (Fig. S1c). In 2000–2010, the mean LOS velocity in the foothills of the southern Santa Cruz Mountains is generally between ±1.5 mm/yr. Since the seasonal variation in deformation rates in the Santa Clara Valley is similar to measured groundwater aquifer levels, we disregard this area for postseismic modeling in order to exclude hydrological deformation (outside of Fig. 3).

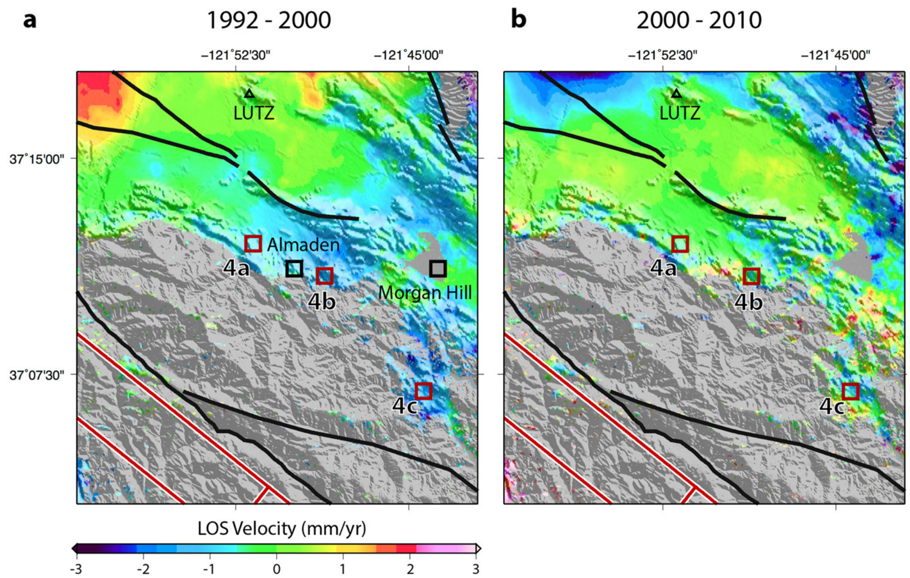

Fig. 3. InSAR line of sight (LOS) velocity during (a) 1992–2000 and (b) 2000–2010. Positive LOS value is range decrease, which represents eastward and/or uplift motion and vise versa. The LOS secular motion is removed based on interseismic dislocation models (Bürgmann, 1997), and the velocity is relative to station LUTZ (black triangle). The black lines are the major fault lines, and the red lines are the coseismic fault geometry by Marshall et al. (1991). The black squares are the nearby towns and the black squares are the locations of time series plots in Fig. 4. (For interpretation of the references to color in this figure legend, the reader is referred to the web version of this article.)

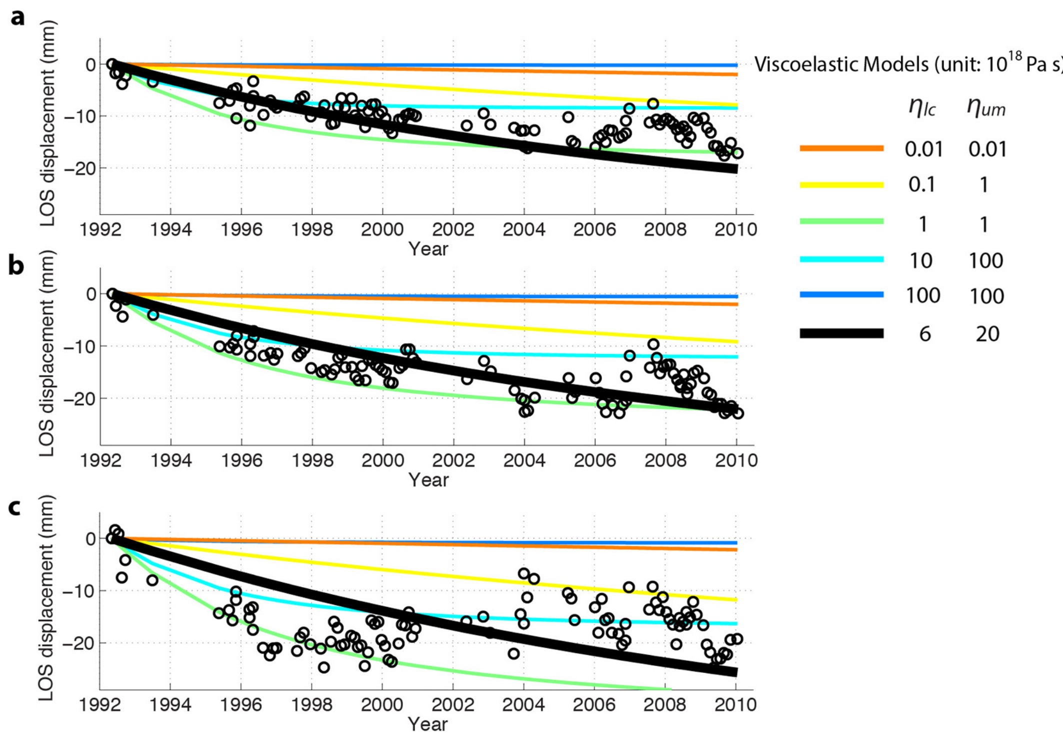

Fig. 4. Selected InSAR time series at points near Loma Prieta region (see Fig. 3 for locations). The circles are the LOS displacements. The colored lines represent different viscoelastic relaxation predictions, and the color index is also shown. The thick black lines show the best-fitting model. (For interpretation of the references to color in this figure legend, the reader is referred to the web version of this article.)

4. Postseismic deformation modeling

We first test the viscoelastic relaxation due to the Loma Prieta coseismic stress change in the lower crust and upper mantle during 1994–2014. Subsequently, we use dislocation models in a layered elastic half-space to calculate afterslip in 1989–1994, 1994–2000, and 2000–present time periods, by inverting the residuals from the viscoelastic model predictions. We invert for distributed afterslip on two fault planes associated with the Loma Prieta fault rupture zone and the Foothills thrust belt, respectively.

4.1. Viscoelastic relaxation (VER)

We use simple elastic dislocation models to compute coseismic stress changes that drive postseismic relaxation in a layered viscoelastic representation of the Earth's lithosphere. By specifying the coseismic fault geometry and slip, and the depth dependent

Table 1
Coseismic fault parameters (after Marshall et al., 1991).

Fault	Length (km)	Width (km)	Strike (°)	Dip (°)	Rake (°)	Slip (m)	Depth (km)	Moment (N m)
Plane 1 (NW)	17	9.1	128	60	116	2.1	9.5–17.4	1.62×10^{19}
Plane 2 (SE)	17	9.1	128	60	163	1.0	9.5–17.4	7.7×10^{18}

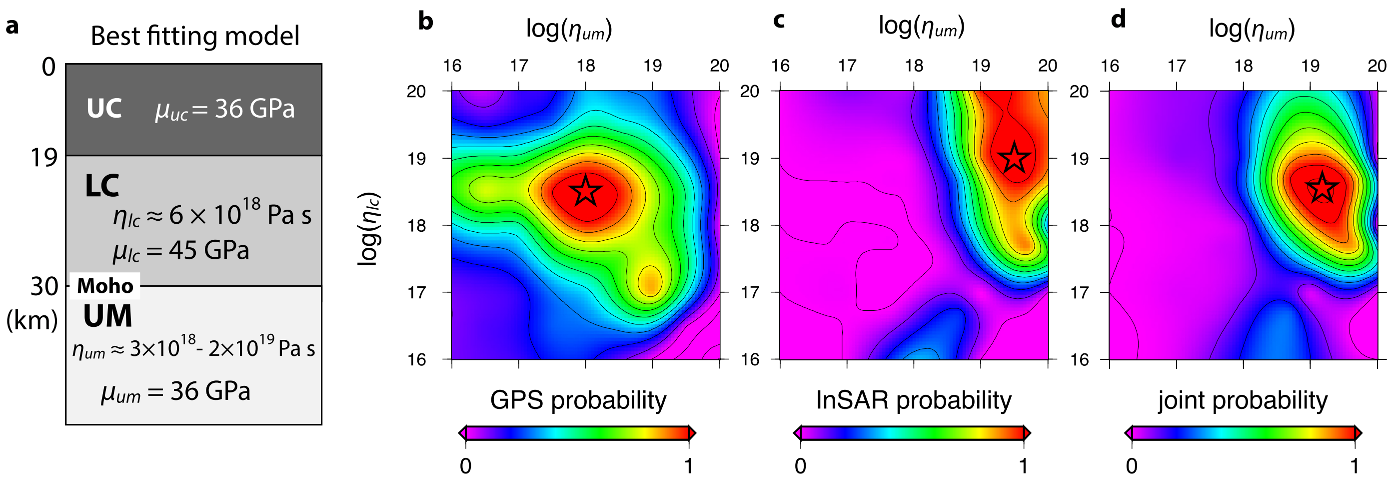

Fig. 5. Viscoelastic relaxation (VER) model. (a) Rheology structure based on the best-fitting model corresponds to the joint probability in (c). (b) Probability density function (PDF) of model fitting to GPS time series and (c) InSAR time series. (d) Joint GPS and InSAR probability density function. (For interpretation of the references to color in this figure legend, the reader is referred to the web version of this article.)

Table 2
Fault geometry for afterslip model (after Bürgmann et al., 1997).

Fault	Length (km)	Bottom depth (km)	Top depth (km)	Strike (°)	Dip (°)	Longitude	Latitude[a]
Plane 1 (Loma Prieta)	53.82	15.57	1.48	130	70	−121.55	36.80
Plane 2 (shallower fault)	61.40	6.11	1.62	132	30	−121.59	36.86

[a] Coordinates are of the center of lower edge of the model fault plane.

elastic and viscous parameters, we can predict the surface displacement in time due to the stress relaxation. We rely on the coseismic fault models of Marshall et al. (1991) and Arnadottir and Segall (1994) to develop a two-dislocation model (Table 1). We use this two sub-fault system to represent a rake transition in slip from nearly right-lateral (163°) in the southeast to oblique right-reverse in the northwest (116°). We follow the coseismic slip model setup in Pollitz et al. (1998) and set the coseismic slip to extend from 9.5 to 17.4 km in depth.

The layered rheologic model is composed of an elastic upper crust underlain by a viscoelastic lower crust and a viscoelastic upper mantle below 30 km depth (Fig. 5a), both with a Maxwell fluid rheology. The thickness of the upper and lower crust is 19 and 11 km, respectively, following Pollitz et al. (1998, 2004). The VISCO1D code (Pollitz, 1992) is used to calculate deformation of the spherically stratified elastic–viscoelastic medium, relying on spheroidal and toroidal motion solutions separable in spherical harmonic degree. We allow for different viscosities of the lower crust and upper mantle, and consider variable viscosity of both layers (η_{lc} for lower crust and η_{um} for upper mantle) between 10^{16} and 10^{20} Pa s. We do not attempt to use the bi-viscous Burgers model (i.e., time dependent viscosity, see Pollitz, 2003) to describe the rapid early postseismic deformation, which was previously found to be dominated by afterslip (Pollitz et al., 1998). It is difficult to separate the contributions of early afterslip and transient VER, so instead we compare linear viscoelastic models with postseismic measurements after 1994.

4.2. Afterslip

As described in Section 4.1, Segall et al. (2000) concluded that afterslip dominates the postseismic displacement until 1994 based on 1989.8–1998 GPS measurements. Here we perform afterslip dislocation inversions to the residuals of the VER models during 1989.8–1994, 1994–2000, and 2000–present, so we can evaluate the contribution of afterslip in the different time periods. We use a two-fault geometry based on the fault parameters found by non-linear inversion of postseismic GPS data in Bürgmann et al. (1997), which was also used in afterslip models of Pollitz et al. (1998) and Segall et al. (2000). One fault roughly coincides with the Loma Prieta earthquake rupture (dipping 70° to the SW), and the other, shallower dipping (30°) fault lies in the Foothills thrust belt (Table 2). For this two-fault system each fault plane is composed of 20×10 subfaults, and the size of each subfault is roughly 3×2 km^2. Each subfault is able to slip with a variable rake along the fault surface but no opening component is allowed, and the smoothing parameter determines the slip variation between subfaults. We extend the main fault down dip to 25 km depth to allow for deep afterslip (Savage and Svarc, 2010) and evaluate the trade-off between deep afterslip and lower-crustal viscosity. We use the programs EDGRN/EDCMP (Wang et al., 2003) for the calculation of the Green's functions relating unit slip on each sub-fault dislocation to surface displacement in a layered elastic model over a half-space, using elastic parameters from Pollitz et al. (1998). The smoothing parameters are determined by the method described in Huang et al. (2013).

5. Modeling results

5.1. Viscoelastic relaxation

To explore the rheologic structure, we perform a grid search for different lower-crustal and upper-mantle viscosities, allowed to vary between 10^{16} and 10^{20} Pa s, and compare the model surface deformation with GPS time series during 1994–2013 and InSAR time series during 1992–2010.

We formulate this problem in a Bayesian framework, and use a likelihood function $p(\mathbf{d}|\mathbf{m})$ to describe how well a model prediction given by specific parameters can explain the observed data (Bodin et al., 2012). The likelihood function for the GPS time series is,

$$p(\mathbf{d}_{\mathrm{GPS}}|\mathbf{m}) = \frac{1}{(2\pi\sigma^2_{k_{i,j}})^{\frac{2MN}{2}}} \times \exp\left[-\frac{1}{2}\Phi_{\mathrm{GPS}}(\mathbf{m})\right], \tag{2a}$$

and

$$\Phi_{\mathrm{GPS}}(\mathbf{m}) = \sum_{k=1}^{M}\sum_{i=1}^{N}\sum_{j=1}^{2}\left[\frac{O_{k_{i,j}} - m_{k_{i,j}}}{\sigma_{k_{i,j}}}\right]^2. \tag{2b}$$

Here $O_{k_{i,j}}$ is the jth component of the ith time step for the kth GPS observation, and $m_{k,i,j}$ is the jth component of the ith time step for the kth model prediction. $\sigma_{k_{i,j}}$ is the uncertainty of the jth component of the ith time step of the kth GPS observation. Here we only consider horizontal measurements so $j = 1, 2$. There are totally 13 GPS stations regularly surveyed since the earthquake, so $k = 13$. The uncertainty of GPS is 3–6 mm for the Segall et al. (2000) dataset, and ∼3 mm for the *USGS* dataset based on uncertainty estimations in their studies. All of the GPS stations locate near the Loma Prieta earthquake region, so even stations east of the Calaveras Fault (e.g. HAMI, MOCH, and OSO1) experience some far-field VER. In addition, there may be displacement residual east of the Calaveras fault due to change of slip rate on the Calaveras fault after the Morgan Hill event (Fig. 2f). As a result, we allow for a systematic, common-mode shift to adjust the E–W and N–S components of all GPS stations to minimize the model residual, and we consider this result as a reference-point-free realization of the postseismic deformation.

The highest probability for GPS data favors a lower-crustal viscosity of $\sim 3 \times 10^{18}$ Pa s and upper-mantle viscosity of $\sim 10^{18}$ Pa s (Fig. 5b), but there is a wide high-probability region (yellow to red color in Fig. 5b) between 10^{17} and 10^{19} Pa s for the upper mantle and between 6×10^{17} and 10^{19} Pa s for the lower crust.

Likewise, the likelihood function of the InSAR time series is,

$$p(\mathbf{d}_{\mathrm{InSAR}}|\mathbf{m}) = \frac{1}{(2\pi)^{MN/2}}|\mathbf{Q}_i|^{-1/2} \times \exp\left[-\frac{1}{2}\Phi_{\mathrm{InSAR}}(\mathbf{m})\right], \tag{3a}$$

and

$$\Phi_{\mathrm{InSAR}}(\mathbf{m}) = \sum_{k=1}^{M}\sum_{i=1}^{N}\left[(\mathbf{o}_{k_i} - \mathbf{m}_{k_i})^T\mathbf{Q}_i^{-1}(\mathbf{o}_{k_i} - \mathbf{m}_{k_i})\right]. \tag{3b}$$

Here O_{ki} and $m_{k,i}$ is the same as Eq. (2), and there is only one velocity component (LOS) so $j = 1$. $\mathbf{Q}_i$ is the variance–covariance matrix that contains the InSAR uncertainty structure. Calculating the InSAR uncertainty structure is non-trivial (e.g. Bekaert et al., 2015) as the noise could be correlated in space due to atmospheric phase noise. In Supplementary Information S4 we provide the method suggested by Sudhaus and Jónsson (2009) to construct $\mathbf{Q}_i$ for each acquisition in Eq. (3). We down-sample the InSAR data into about one point per km^2 and only consider points near the Loma Prieta region (area shown in Fig. 3). We also exclude areas that experience substantial seasonal variation associated with hydrology (Fig. S5a), in particular in the Santa Clara Valley (Fig. S1), and there are 638 points left after this process. As shown in Fig. 5c, VER with a lower crustal viscosity (η_{lc}) higher than $\sim 5 \times 10^{17}$ Pa s and upper mantle viscosity (η_{um}) $\sim 3 \times 10^{19}$ Pa s can explain the InSAR time series well. The best fitting relaxation model matches the longer-term trend in the time series (Fig. 4).

The joint likelihood function (Bodin et al., 2012) of the GPS and InSAR datasets is,

$$p(\mathbf{d}_{joint}|\mathbf{m}) = p(\mathbf{d}_{\mathrm{GPS}}|\mathbf{m}) \times p(\mathbf{d}_{\mathrm{InSAR}}|\mathbf{m}) \\ \propto \exp\left\{-\frac{1}{2}\left[\Phi_{\mathrm{GPS}}(\mathbf{m}) + \Phi_{\mathrm{InSAR}}(\mathbf{m})\right]\right\}, \tag{4}$$

where the joint probability is the product of the likelihood functions for GPS and InSAR datasets. In this way, the relative contribution of the two datasets to the joint likelihood distribution is directly determined by data errors, so no user-defined weighting factor is needed in the inversion. Fig. 5d shows the joint probability distribution. The result shows a similar distribution as for the InSAR data, but the region with high probability is more confined. Fig. S7 shows the joint probability distribution with different InSAR weighting. The highest probability of upper mantle viscosity decreases from $\sim 2 \times 10^{19}$ to $\sim 3 \times 10^{18}$ Pa s when decreasing InSAR weighting, while the preferred lower-crustal viscosity remains $\sim 6 \times 10^{18}$ Pa s. Fig. 6a–c compares the best-fitting VER model with the average GPS velocities in 1989–1994, 1994–2000, and 2000–present and Fig. 6d and Fig. S2 show fits to the time series of total horizontal displacements for a range of lower-crustal and upper-mantle viscosities considered.

Alternatively, we consider GPS data from Bürgmann et al. (1997), d'Alessio et al. (2005), and continuous and campaign USGS data (http://earthquake.usgs.gov/monitoring/gps/) to represent the 1989–1994, 1994–2003, and 2000–present time periods, respectively. We perform the same approach and the results are shown in Fig. S6. As we only consider post-1994 GPS data when determining the model misfit, the best fitting model strongly underestimates the observed 1989–1994 displacement, which we attribute to early afterslip. After 2000, the modeled postseismic velocities generally drop to below 2 mm/yr. The higher VER misfit in 1989–1994 implies additional processes to explain the early stage of postseismic displacement. In addition, we take the best-fitting VER model to predict station-pair length change (green lines in Fig. 2). We do not include baseline-length change data in model fitting because the post-Loma Prieta measurements are GPS based so already included in the viscoelastic modeling. The viscoelastic relaxation prediction agrees well with length change measurements except for ALLI–LOMA (Fig. 2d). The opposite length change is because both ALLI and LOMA move southeastward and the lengthening is due to further southwestward motion at LOMA. In the predicted relaxation, LOMA has slightly northward movement whereas southward at ALLI, and hence predicting shortening.

5.2. Afterslip inversion

For afterslip inversions, we extend the Loma Prieta fault to 25 km depth to allow for the contribution of afterslip in the lower-crust down-dip of the coseismic rupture (Savage and Svarc, 2010) and examine the tradeoff between lower-crustal viscosity and deep-seated afterslip. In order to estimate the afterslip component, we use the VER model residuals of GPS and InSAR datasets during the 1989–1994, 1994–2000, and 2000–present periods as dislocation inversion inputs. The upper-mantle viscosity is fixed at 2×10^{19} Pa s, whereas the lower-crustal viscosity varies from 5×10^{16} to 10^{20} Pa s. We calculate the reduced χ^2 misfit of each

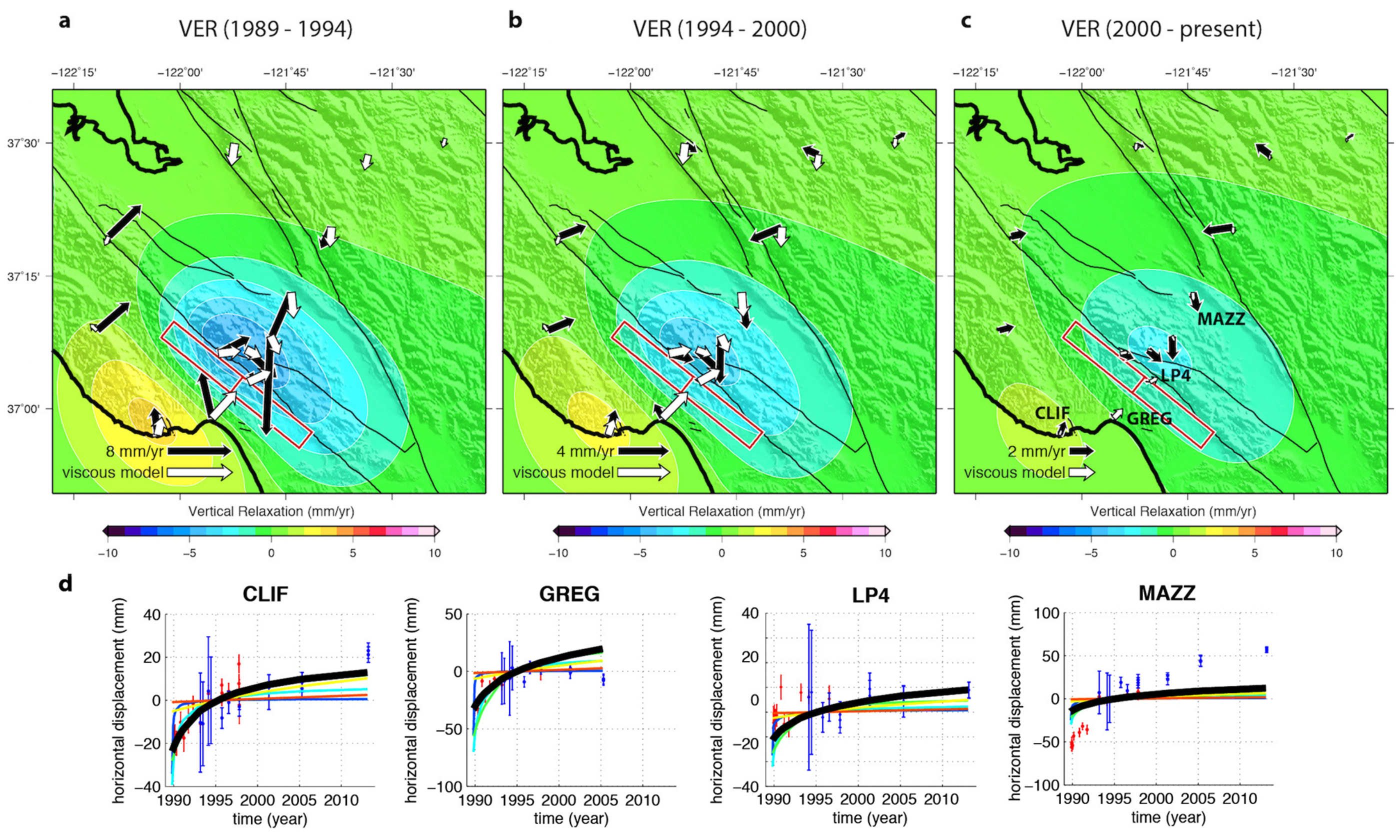

Fig. 6. Viscoelastic relaxation (VER) model in (a) 1989–1994, (b) 1994–2000, and (c) 2000–present time periods. The black arrows show GPS postseismic displacement after correcting for a common shift in E–W and N–S components to minimize model misfit (see text) in different time periods based on Eq. (1), and the white arrows are VER predictions due to stress change from coseismic slip on the fault planes (red rectangles). The background colors are vertical viscoelastic predictions. (d) Selected GPS stations (see Fig. S2b for fitting to all stations) in horizontal time series. The colored lines represent different viscoelastic model (the same color-code as Fig. 4). (For interpretation of the references to color in this figure legend, the reader is referred to the web version of this article.)

afterslip-viscoelastic relaxation model to evaluate model fitting. The χ^2 misfit is defined:

$$\chi^2 = \frac{1}{MNP}\sum_{k=1}^{M}\sum_{i=1}^{N}\sum_{j=1}^{P}\frac{(o_{k_{i,j}} - m_{k_{i,j}})^2}{\sigma_{i,j,k}^2}, \tag{5}$$

where notations the same as Eq. (2b).

Fig. S8 shows afterslip distributions and the (reduced) χ^2 misfit for a range of lower-crustal viscosities. The result suggests more deep afterslip appeared when lower-crustal viscosity is higher. Fig. 7 shows afterslip distribution and fitting to GPS with the best fitting lower-crustal viscosity (6×10^{18} Pa s). In the 1989–1994 time period, the GPS χ^2 misfit is 16.4 when solely using the VER model (black arrows in Fig. 7a), and the χ^2 misfit is 3.0 and 1.4 in the 1994–2000 and 2000–present period, respectively. Overall the improvement in fit from the addition of afterslip is better near the Loma Prieta region than the far-field regions (PAWT, EAUN, and stations east of Calaveras Fault).

The χ^2 misfit of the afterslip inversion is 3.2 for 1989–1994, 1.04 for 1994–2000, and 0.5 for 2000–present. They are all smaller than the viscoelastic model chi-square misfits because it is taking VER residual as data input, so the $(o_k - m_k)^2$ term of afterslip models in Eq. (5) is generally lower. The dislocation inversions in Fig. 7d–f show shallow oblique right-lateral strike–slip on the Loma Prieta fault and dip–slip dominated afterslip in the northwestern portion of the Foothills thrust in all time periods. This strike–slip dominated Loma Prieta fault afterslip and dip–slip dominated Foothills thrust afterslip is similar to the pattern obtained by Segall et al. (2000). Alternatively, we perform the same afterslip inversion to the VER model residuals of GPS data (Fig. S6) from Bürgmann et al. (1997), d'Alessio et al. (2005), and recent USGS solutions of campaign and continuous GPS data to represent the 1989–1994, 1994–2003, and 2000–present time periods. The results for these larger datasets are shown in Fig. S8 and the χ^2 misfit are 3.9, 1.2, and 1.7 for the 1989–1994, 1994–2003, and 2000–present time period, respectively.

6. Discussion

6.1. Early to late period Loma Prieta postseismic deformation

Fitting logarithmic functions (Eq. (1)) to the GPS time series, there is an azimuthal change in the postseismic displacement close to the Loma Prieta epicenter between the early and the late periods that might imply a change of source mechanism (Fig. 1b). Combining both VER and afterslip mechanisms we can explain the GPS data well in all time periods near the Loma Prieta region (Fig. 8). The VER model also predicts a range increase in InSAR LOS (Fig. 8b) in the 1992–2000 time period that agrees with observed LOS increase (Figs. 3 and 4). These results are consistent with a change of dominant relaxation mechanism from afterslip (Bürgmann et al., 1997; Pollitz et al., 1998; Segall et al., 2000) and/or fault zone collapse (Savage et al., 1994; Savage and Svarc, 2010) in the early postseismic period to VER in the later period. The total moment of the 1989–1994 afterslip is equivalent of M_w 6.3, about 11.5% of the coseismic moment. We cannot rule out the contribution of afterslip during 1994–2000, or even after 2000 (Figs. 7 and S8).

Postseismic deformation fitting in the later stage (2000 to present) remains challenging because the postseismic transient is

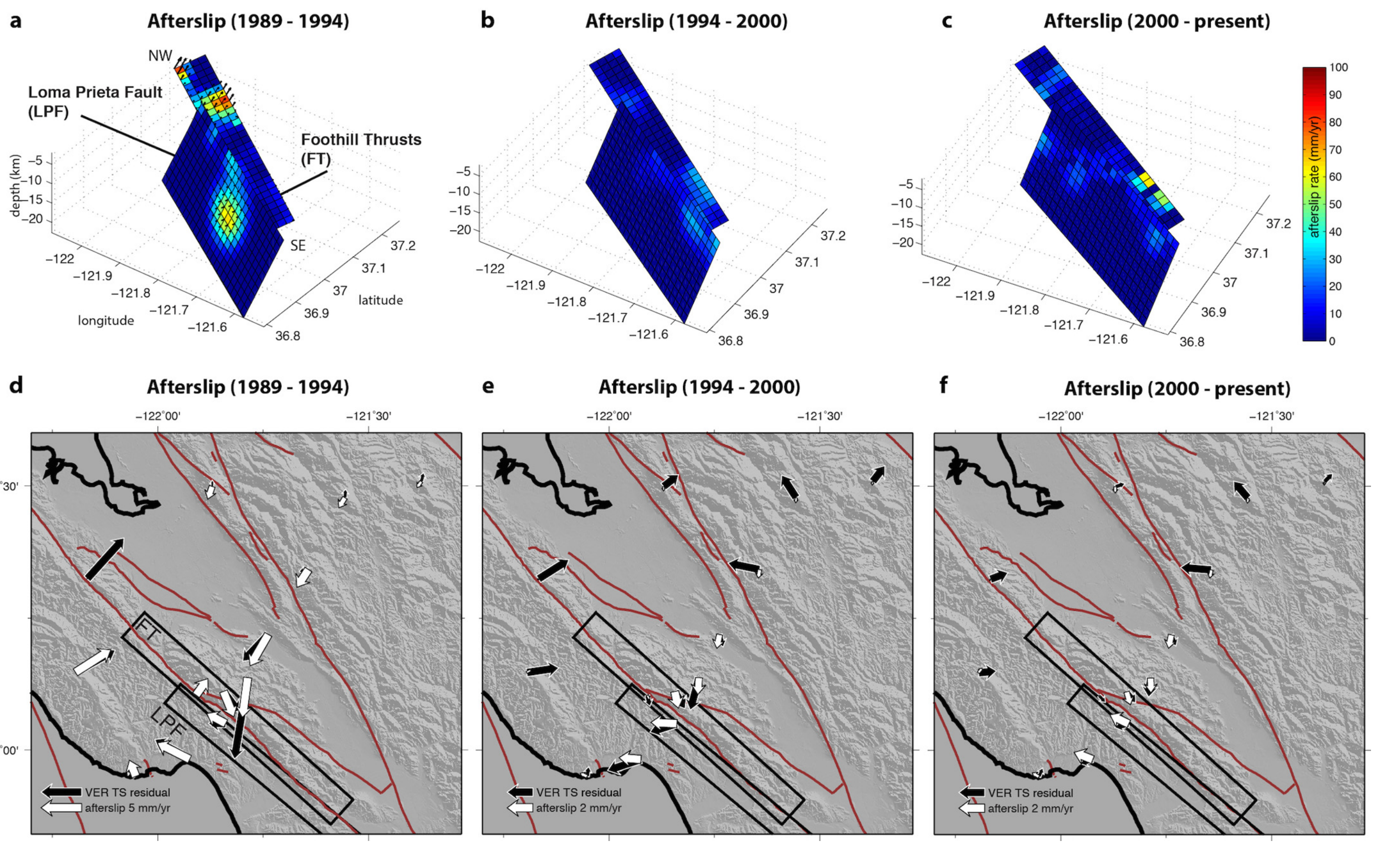

Fig. 7. Inverted afterslip distribution on each fault planes in (a) 1989–1994, (b) 1994–2000, and (c) 2000–present time periods. The fault geometries are based on Bürgmann et al. (1997). The orientation of the black arrows indicate rake. (d–f) Afterslip predicted surface displacement from the two faults. The black arrows are viscoelastic model misfits (the residuals in Fig. 6) and white arrows are afterslip prediction.

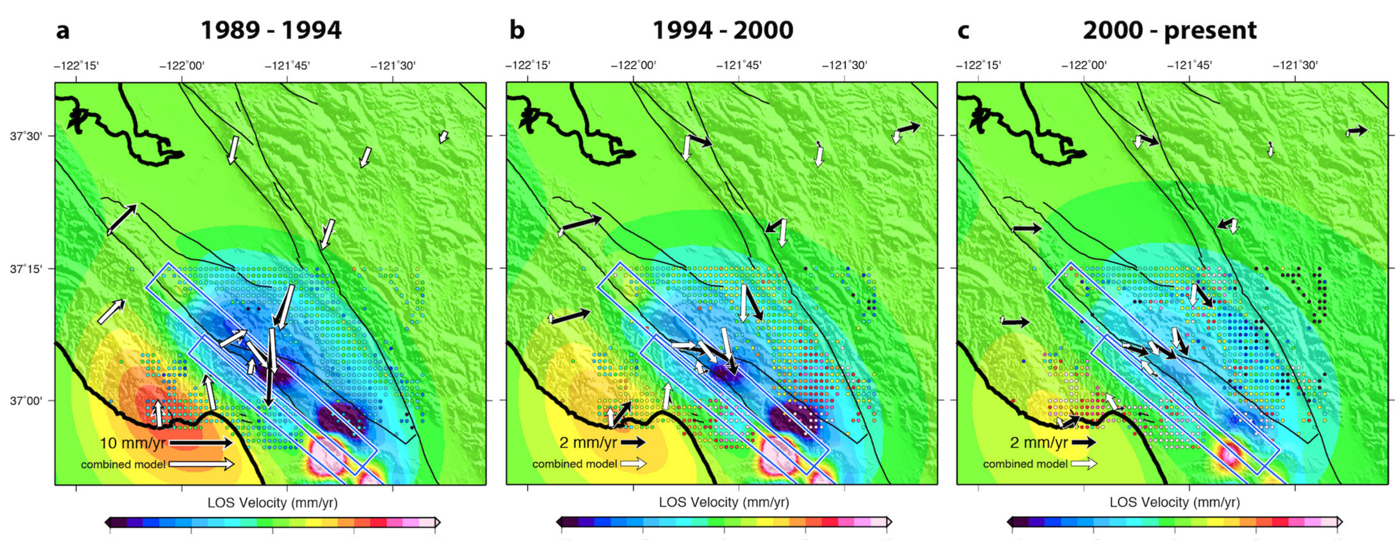

Fig. 8. Viscoelastic relaxation and afterslip combined model fitting to GPS data in (a) 1989–1994, (b) 1994–2000, and (c) 2000–present time periods. The black arrows are GPS postseismic displacements in different time periods, and the white arrows are the multiple-mechanism models in different time periods. The background colors show the predicted surface relaxation prediction in LOS, and the black outlined circles are InSAR velocity in each time periods. (For interpretation of the references to color in this figure legend, the reader is referred to the web version of this article.)

increasingly difficult to separate from the interseismic secular motion. In the study area there were no long-term GPS measurements prior to the Loma Prieta earthquake, so we rely on the interseismic secular motion model by Bürgmann (1997), which is inverted from pre-Loma Prieta earthquake trilateration surveys (Lisowski et al., 1991). As shown in Fig. 2f, the 1984 Morgan Hill earthquake influenced part of the interseismic model, and additionally we cannot rule out the possibility of un-modeled interseismic motion, which may contribute to uncertainties of our postseismic deformation time series. This may explain the poorer later-stage postseismic GPS fitting (Fig. 6). Likewise, since there is no pre-Loma Prieta InSAR data, we also rely on the same interseismic model to remove the interseismic LOS contribution throughout the entire InSAR time series, so the interseismic model error could again result in a bias for the later postseismic period.

6.2. Afterslip in different time periods

Savage and Svarc (2010) postulated that most of the postseismic displacement in the first 3 years can be attributed to a 1.56 m right-lateral and 0.6 m reverse afterslip on the downdip extension (depth range 16 to 21 km) of the Loma Prieta earthquake fault. In addition, they propose a 0.11 m postseismic fault zone collapse (fault-normal displacement) of the rupture zone (depth ranges 5 to 16 km). Bürgmann et al. (1997) combined 5 yr of GPS and leveling measurements and suggested about 2.9 cm/yr uniform oblique-reverse afterslip on the Loma Prieta fault plane and 2.4 cm/yr uniform reverse afterslip on a buried fault within the Foothills thrust belt.

In this study, we do not allow opening (fault zone collapse) along the fault planes, so the dislocation prediction (white arrows in Fig. 7a) is solely due to afterslip on the fault planes. The amount of deep afterslip in the 1989–1994 period strongly depends on the choice of lower-crustal viscosity, and there is a clear tradeoff between lower-crustal viscosity and the amount of deep afterslip (Fig. S8). The inverted afterslip model can fit the VER model residual when lower-crustal viscosity is higher than 5×10^{17} Pa s, so we cannot separate the afterslip or the lower-crustal relaxation contribution in the early postseismic period. Nevertheless, based on the best fitting model, afterslip dominates at the depth between 8 and 15 km during 1989–1994 (Fig. 7d) and falls to below 3 cm/yr afterwards (Fig. 7e & f). In the Foothills thrust, the peak afterslip based on the 13 GPS stations time series is about 80 mm/yr, but is inconsistent with the result using GPS data from Bürgmann et al. (1997) (Fig. S9a). This is possibly due to different number of geodetic constraints. Besides, it is difficult to directly compare afterslip with previous studies (e.g. Bürgmann et al., 1997; Segall et al., 2000) because we invert the VER model residuals instead of postseismic deformation.

Fig. 8 compares the predicted postseismic deformation from both afterslip and VER. At later time periods (1994–2000 and 2000–present) the relatively uncertain GPS velocities of PAWT and EAUN (2–5 mm/yr) NW of the Loma Prieta fault may map into afterslip in the NW section of the Foothills thrust, leading to small-scale model LOS change not observed in InSAR (Fig. 4).

6.3. Constraining lithospheric rheology

Recent studies (e.g. Hearn et al., 2002; Johnson et al., 2009; Barbot and Fialko, 2010; Bruhat et al., 2011; Rousset et al., 2012; Pollitz, 2015; Rollins et al., 2015) have explored the afterslip-and-viscoelastic-relaxation coupling model that could potentially separate the contributions of the two mechanisms by jointly inverting both mechanisms. In this study, since afterslip dominated the first 5 years of postseismic deformation (Segall et al., 2000), we focus on using post-1994 measurements for exploring lower-crustal and upper mantle viscosities.

The best-fitting VER model suggests that the viscosities of the lower crust and upper mantle are 6×10^{18} Pa s and 3×10^{18}–2×10^{19} Pa s, respectively (Fig. 5d). The viscosity of the upper mantle estimated in this study is consistent with Pollitz et al. (1998) ($\sim 10^{19}$ Pa s), Kenner and Segall (2003) (3×10^{19}–4×10^{19} Pa s), and Pollitz et al. (2004) (10^{19} Pa s), but higher than Johnson and Fukuda (2010) (4×10^{18} Pa s) for the San Francisco Bay Area. Other studies for upper mantle viscosity in southern California also infer a range of 6×10^{18}–3×10^{19} Pa s (Freed and Bürgmann, 2004; Behr and Hirth, 2014). A recent study by Smith-Konter et al. (2014) using tide gauge data to constrain interseismic vertical deformation also predicts asthenosphere viscosity of $\sim 10^{19}$ Pa s. For the lower crust, the viscosity estimated in this study is ~1.6 times lower than in Pollitz et al. (1998) ($\sim 10^{19}$ Pa s), and also lower than values obtained from a range of observations in the western United States (10^{19}–10^{21} Pa s) (Thatcher and Pollitz, 2008). As described in Section 6.2, we may have underestimated the lower-crustal viscosity because we cannot separate VER and afterslip well when the lower-crustal viscosity is higher than 5×10^{17} Pa s. In addition, part of the early inferred deep afterslip might be due to a transient lower-crustal viscosity (Pollitz, 2003; Freed et al., 2012; Huang et al., 2014).

Our modeling approach could potentially bias the estimate of the early VER contribution. However, we only consider post-1994 geodetic data for VER fitting, in which the contribution of afterslip is likely to be negligible (Segall et al., 2000). The low quality of data collected in the early 90s does not allow for incorporating higher-order viscous flow or rate-state fault rheologies. The main challenge of constraining lithospheric rheology here stems from the limited constraints on the pre-earthquake measurements, lower precision of geodetic measurements in the early 1990s, and relatively modest postseismic VER generated by a M_w 6.9 earthquake. We consolidate GPS measurements from Segall et al. (2000), d'Alessio et al. (2005), and the USGS campaign survey (1994–2013) and continuous BARD (1990s–present) and PBO (~2006–present) stations, but some of the stations were established after the earthquake, whereas others were discontinued afterwards. On the other hand, the afterslip-dominated early postseismic deformation does not allow us to easily discern a likely early VER signal in the GPS time series, and therefore we are unable to investigate a time-dependent viscosity such as a bi-viscous Burgers rheology (Pollitz, 2003).

6.4. Accelerated aseismic slip along the San Andreas fault

Turner et al. (2013) document repeating earthquake activity along aseismically creeping sections of the San Andreas and the Sargent faults near San Juan Bautista, southeast of the Loma Prieta rupture zone. They estimated the aseismic slip rate of both faults based on the repeater activity, and found that the San Andreas creep rate fell back to the pre-Loma Prieta slip rate only about 10 yr after the event, consistent with results from creepmeters in the area (Bokelmann and Kovach, 2003).

Near San Juan Bautista, our VER model shows a decrease of differential stressing rate from ~3 kPa/yr in 1990 to ~1.5 kPa/yr at 10 km depth in 1999 (Fig. S11). This VER decay is similar to the observed decay of slip rate along the San Andreas fault (Turner et al., 2013), and hence provides a source that drives the enduring decay of the fault creep and the repeating earthquakes on the creeping segment of the San Andreas fault. Accelerated aseismic slip on the creeping San Andreas fault in the aftermath of large earthquakes on the adjoining locked sections may account for the apparent interseismic slip deficit along this section of the fault (Ryder and Bürgmann, 2008) and may play a role in stress transfer across the central San Andreas fault (Ben-Zion et al., 1993; Lynch et al., 2003).

7. Conclusion

More than two decades of deformation measurements following the 1989 Loma Prieta earthquake document that the postseismic displacement rates fell from >4 cm/yr to millimeter-per-year levels since 2000. Based on dislocation modeling, afterslips on the fault that ruptured in the earthquake and a buried fault within the Foothill thrust belt dominate the rapid early postseismic deformation. Our modeling using a 1D viscoelastic structure composed of an elastic upper crust and Maxwell viscoelastic lower crust and upper mantle, implies that the viscosities of the lower crust and upper mantle are about 6×10^{18} Pa s and 3×10^{18}–2×10^{19} Pa s, respectively. A combined afterslip-viscoelastic model can better explain early and late Loma Prieta postseismic deformation, where the afterslip is reduced in the later period. Our geodetic measurements cannot tightly resolve lithospheric viscosity due to the low amount of the postseismic displacement from this M_w 6.9 earthquake and higher data uncertainty in the early 1990s. The enduringly accelerated activity of repeating earthquakes and fault creep on the San Andreas fault and the Sargent fault after the Loma Prieta earthquake is coherent in time with the modeled postseismic deformation. While early afterslip on the creeping SAF relieved static coseismic stress increases, the added loading due to postseismic shear below the creeping section appears to have lead to more enduring creep-rate increases. This suggests that viscoelastic relaxation could be the source to drive accelerated shallow slip on these creeping faults following the Loma Prieta earthquake.

Acknowledgements

We would like to thank D. Dreger, T. Bodin, I. Johanson, E. Chaussard, C. Johnson, and R. Turner for discussion and constructive suggestions. We thank James Savage and Eileen Evans for reviewing an earlier version of this paper. Two anonymous reviewers give critical and constructive comments on improving the manuscript. All of the USGS GPS campaign and continuous stations data are downloaded from the USGS website (http://earthquake.usgs.gov/monitoring/gps/). Continuous GPS data are from the BARD network and the Plate Boundary Observatory operated by UNAVCO for Earthscope (http://www.earthscope.org). The ERS and Envisat SAR data are copyrighted by the European Space Agency and were provided through the WInSAR archive at UNAVCO. This project is supported by the National Science Foundation grant (EAR-0951430) and NASA (NXX08AG50G). M.-H. Huang is supported by an appointment to the NASA Postdoctoral Program at the Jet Propulsion Laboratory, administered by Oak Ridge Associated Universities through a contract with NASA. This is Berkeley Seismological Laboratory contribution #2015-10. The research was carried out at the Jet Propulsion Laboratory, California Institute of Technology, under a contract with the National Aeronautics and Space Administration.

Appendix A. Supplementary material

Supplementary material related to this article can be found online at http://dx.doi.org/10.1016/j.epsl.2015.12.018.

References

Arnadottir, T., Segall, P., 1994. The 1989 Loma Prieta earthquake imaged from inversion of geodetic data. J. Geophys. Res. 99, 21,835–21,855.

Barbot, S., Fialko, Y., 2010. A unified continuum representation of post-seismic relaxation mechanisms: semi-analytic models of afterslip, poroelastic rebound and viscoelastic flow. Geophys. J. Int. 182, 1124–1140.

Behr, W., Hirth, G., 2014. Rheological properties of the mantle lid beneath the Mojave region in southern California. Earth Planet. Sci. Lett. 393, 60–72.

Bekaert, D.P.S., Hooper, A., Wright, T.J., 2015. Reassessing the 2006 Guerrero slow-slip event, Mexico: implications for large earthquakes in the Guerrero Gap. J. Geophys. Res., Solid Earth 120, 1357–1375. http://dx.doi.org/10.1002/2014JB011557.

Ben-Zion, Y., Rice, J.R., Dmowska, R., 1993. Interaction of the San Andreas fault creeping segment with adjacent great rupture zones and earthquake recurrence at Parkfield. J. Geophys. Res., Solid Earth 98 (B2), 2135–2144.

Berardino, P., Fornaro, G., Lanari, R., Sansosti, E., 2002. A new algorithm for surface deformation monitoring based on small baseline differential SAR interferograms. IEEE Trans. Geosci. Remote Sens. 40, 2375–2383.

Bodin, T., Sambridge, M., Tkalčić, H., Arroucau, P., Gallagher, K., Rawlinson, N., 2012. Transdimensional inversion of receiver functions and surface wave dispersion. J. Geophys. Res. 117, B02301.

Bokelmann, G.H.R., Kovach, R.L., 2003. Long-term creep-rate changes and their causes. Geophys. Res. Lett. 30, 1445.

Bruhat, L., Barbot, S., Avouac, J.-P., 2011. Evidence for postseismic deformation of the lower crust following the 2004 M_w 6.0 Parkfield earthquake. J. Geophys. Res. 116, B08401.

Bürgmann, R., 1997. Active detachment faulting in the San Francisco Bay area? Geology 25, 1135–1138.

Bürgmann, R., Dresen, G., 2008. Rheology of the lower crust and upper mantle: evidence from rock mechanics, geodesy and field observations. Annu. Rev. Earth Planet. Sci. 36, 531–567.

Bürgmann, R., Hilley, G., Ferretti, A., Novali, F., 2006. Resolving vertical tectonics in the San Francisco Bay area from GPS and Permanent Scatterer InSAR analysis. Geology 34, 221–224.

Bürgmann, R., Segall, P., Lisowski, M., Svarc, J., 1997. Postseismic strain following the 1989 Loma Prieta earthquake from GPS and leveling measurements. J. Geophys. Res. 102, 4933–4955.

Chaussard, E., Bürgmann, R., Shirzaei, M., Fielding, E.J., Baker, B., 2014. Predictability of hydraulic head changes and characterization of aquifer system and fault properties from InSAR-derived ground deformation. J. Geophys. Res., Solid Earth 119, 6572–6590. http://dx.doi.org/10.1002/2014JB0011266.

Chen, C.W., Zebker, H.A., 2002. Phase unwrapping for large SAR interferograms: statistical segmentation and generalized network models. IEEE Trans. Geosci. Remote Sens. 40 (8), 1709–1719.

d'Alessio, M.A., Johanson, I.A., Bürgmann, R., Schmidt, D.A., Murray, M.H., 2005. Slicing up the San Francisco Bay Area: block kinematics and fault slip rates from GPS-derived surface velocities. J. Geophys. Res. 110. http://dx.doi.org/10.1029/2004JB003496.

Fielding, E., Lundgren, P.R., Bürgmann, R., Gareth, F.J., 2009. Shallow fault-zone dilatancy recovery after the 2003 Bam earthquake in Iran. Nature 458, 64–68.

Freed, A.M., Bürgmann, R., 2004. Evidence of power-law flow in the Mojave desert mantle. Nature 430, 548–551. http://dx.doi.org/10.1038/nature02784.

Freed, A.M., Hirth, G., Behn, M.D., 2012. Using short-term postseismic displacements to infer the ambient deformation conditions of the upper mantle. J. Geophys. Res. 117, B01409. http://dx.doi.org/10.1029/2011JB008562.

Hearn, E.H., Bürgmann, R., Reilinger, R., 2002. Dynamics of Izmit earthquake postseismic deformation and loading of the Duzce earthquake hypocenter. Bull. Seismol. Soc. Am. 92, 172–193.

Henstock, T.J., Levander, A., Hole, J.A., 1997. Deformation in the lower crust of the San Andreas fault system in northern California. Science 278, 650–653.

Huang, M.-H., Dreger, D., Bürgmann, R., Yoo, S.-H., Hashimoto, M., 2013. Joint inversion of seismic and geodetic data for the source of the 2010 March 4, M_w 6.3 Jia-Shian, SW Taiwan, earthquake. Geophys. J. Int. 193, 1608–1626. http://dx.doi.org/10.1093/gji/ggt058.

Huang, M.-H., Bürgmann, R., Freed, A.M., 2014. Probing the lithospheric rheology across the eastern margin of the Tibetan Plateau. Earth Planet. Sci. Lett. 39, 88–96. http://dx.doi.org/10.1016/j.epsl.2014.04.003.

Johanson, I.A., Bürgmann, R., 2005. Creep and quakes on the northern transition zone of the San Andreas fault from GPS and InSAR data. Geophys. Res. Lett. 32. http://dx.doi.org/10.1029/2005GL023150.

Johnson, K.M., Bürgmann, R., Freymueller, J.T., 2009. Coupled afterslip and viscoelastic flow following the 2002 Denali Fault, Alaska Earthquake. Geophys. J. Int. 176. http://dx.doi.org/10.1111/j.1365-1246X.2008.04029.x.

Johnson, K.M., Bürgmann, R., Larson, K., 2006. Frictional properties on the San Andreas fault near Parkfield, California, inferred from models of afterslip following the 2004 earthquake. Bull. Seismol. Soc. Am. 96, 321–338.

Johnson, K.M., Fukuda, J., 2010. New methods for estimating the spatial distribution of locked asperities and stress-driven interseismic creep on faults with application to the San Francisco Bay Area, California. J. Geophys. Res. 115, B12408. http://dx.doi.org/10.1029/2010JB007703.

Jónsson, S., Segall, P., Pedersen, R., Björnsson, G., 2003. Post-earthquake ground movements correlated to pore-pressure transients. Nature 424, 179–183.

Kenner, S.J., Segall, P., 2003. Lower crustal structure in northern California: implications from strain-rate variations following the 1906 San Francisco earthquake. J. Geophys. Res. 108. http://dx.doi.org/10.1029/2001JB000189.

Lisowski, M., Savage, J.C., Prescott, W.H., 1991. The velocity field along the San Andreas fault in central and southern California. J. Geophys. Res. 96, 8369–8389.

Lynch, J.C., Bürgmann, R., Richards, M.A., Ferencz, R.M., 2003. When faults communicate: viscoelastic coupling and earthquake clustering in a simple two-fault strike–slip system. Geophys. Res. Lett. 30. http://dx.doi.org/10.1029/2002GL016765.

Marshall, G.A., Stein, R.S., Thatcher, W., 1991. Faulting geometry and slip from co-seismic elevation changes: the 18 October 1989, Loma Prieta, California, earthquake. Bull. Seismol. Soc. Am. 81, 1660–1693.

Peltzer, G., Rosen, P., Rogez, F., Hudnut, K., 1996. Postseismic rebound in fault step-overs caused by pore fluid flow. Science 273, 1202–1204.

Pollitz, F., 1992. Postseismic relaxation theory on the spherical Earth. Bull. Seismol. Soc. Am. 82, 422–453.

Pollitz, F., 2015. Post-earthquake relaxation evidence for laterally variable viscoelastic structure and water content in the southern California mantle. J. Geophys. Res. 120, 2672–2696. http://dx.doi.org/10.1002/2014JB011603.

Pollitz, F., Bürgmann, R., Segall, P., 1998. Joint estimation of afterslip rate and postseismic relaxation following the 1989 Loma Prieta earthquake. J. Geophys. Res. 103, 26,975–26,992.
Pollitz, F.F., 2003. Transient rheology of the uppermost mantle beneath the Mojave Desert, California. Earth Planet. Sci. Lett. 215, 89–104. http://dx.doi.org/10.1016/S0012-821X(03)00432-1.
Pollitz, F., Bakun, W.H., Nyst, M., 2004. A physical model for strain accumulation in the San Francisco Bay region: stress evolution since 1838. J. Geophys. Res. 109, B11408. http://dx.doi.org/10.1029/2004JB003003.
Rollins, Christopher, Barbot, Sylvain, Avouac, Jean-Philippe, 2015. Postseismic deformation following the 2010 $M = 7.2$ El Mayor-Cucapah earthquake: observations, kinematic inversions, and dynamic models. Pure Appl. Geophys. 172, 1305–1358.
Rosen, P.A., Hensley, S., Peltzer, G., 2004. Updated repeat orbit interferometry package released. Eos 85 (5), 47.
Rousset, Baptiste, et al., 2012. Postseismic deformation following the 1999 Chi-Chi earthquake, Taiwan: implication for lower-crust rheology. J. Geophys. Res., Solid Earth (1978–2012) 117 (B12).
Ryder, I., Bürgmann, R., 2008. Spatial variations in slip deficit on the central San Andreas Fault from InSAR. Geophys. J. Int. 175, 837–852. http://dx.doi.org/10.1111/j.1365-246X.2008.03938.x.
Savage, J.C., Lisowski, M., Svarc, J.L., 1994. Postseismic deformation following the 1989 ($M = 7.1$) Loma Prieta, California, earthquake. J. Geophys. Res. 99, 13757–13765.
Savage, J.C., Svarc, J.L., 2010. Postseismic relaxation following the 1989 M_s 7.1 Loma Prieta earthquake, central California. J. Geophys. Res. 115, B08404.
Schmidt, D.A., Bürgmann, R., 2003. Time dependent land uplift and subsidence in the Santa Clara valley, California, from a large InSAR data set. J. Geophys. Res. 108. http://dx.doi.org/10.1029/2002JB002267.
Segall, P., Bürgmann, R., Matthews, M., 2000. Time dependent deformation following the 1989 Loma Prieta earthquake. J. Geophys. Res. 105, 5615–5634.
Smith-Konter, B.R., Thornton, G.M., Sandwell, D.T., 2014. Vertical crustal displacement due to interseismic deformation along the San Andreas fault: constraints from tide gauges. Geophys. Res. Lett. 41, 3793–3801.
Sudhaus, H., Jónsson, S., 2009. Improved source modeling through combined use of InSAR and GPS under consideration of correlated data errors: application to the June 2000 Kleifarvatn earthquake, Iceland. Geophys. J. Int. 176, 389–404. http://dx.doi.org/10.1111/j.1365-246X.2008.03989.x.
Thatcher, W., Pollitz, F., 2008. Temporal evolution of continental lithospheric strength in actively deforming regions. GSA Today 18. http://dx.doi.org/10.1130/GSAT01804-5A.1.
Tse, S.T., Rice, J.R., 1986. Crustal earthquake instability in relation to the depth variation of frictional slip properties. J. Geophys. Res. 91 (B9), 9452–9472. http://dx.doi.org/10.1029/JB091iB09p09452.
Turner, R.C., Nadeau, R.M., Bürgmann, R., 2013. Aseismic slip and fault interaction from repeating earthquakes in the Loma Prieta aftershock zone. Geophys. Res. Lett. 40, 1079–1083. http://dx.doi.org/10.1002/grl.50212.
USGS website, 2015. http://earthquake.usgs.gov/monitoring/gps/SFBayArea_SGPS.
Wang, R., Lorenzo Martín, F., Roth, F., 2003. Computation of deformation induced by earthquakes in a multi-layered elastic crust-FORTRAN programs EDGRN/EDCMP. Comput. Geosci. 29, 195–207.

Viscous post 1989 M_w 6.9 Loma Prieta earthquake relaxation revealed from GPS and InSAR Data

Mong-Han Huang[1,2,4*], Roland Bürgmann[1,2], Fred Pollitz[3]

[1]Department of Earth and Planetary Science, University of California, Berkeley, California, 94720-4767, USA

[2]Berkeley Seismological Laboratory, University of California, Berkeley, California, 94720-4767, USA

[3]U.S. Geological Survey, 345 Menlo Park, California, 94025, USA

[4]Now at Jet Propulsion Laboratory, California Institute of Technology, 4800 Oak Grove Drive, Pasadena, California 91109, USA

*Corresponding author. Tel. +1 818 354 4456.

E-mail address: mong@seismo.berkeley.edu (M.-H. Huang)

Supplementary Information

S1. Baseline-length measurements between HAML, LOMA, and AMER

To explore whether or not the interseismic slip rate of the Calaveras fault segment near Morgan Hill requires an adjustment for the 1984 earthquake, we further examine the distance change between pairs HAML – LOMA (Fig. S3a-b), HAML – AMER (Fig. S3c) and LOMA – AMER (Fig. S3d-f), where AMER is west of the Calaveras fault. The BARD GPS station LUTZ was built near AMER and surveyed continuously since 1996 (Fig. 1a), and MHCB is close to HAML and surveyed continuously since 2000.

For HAML – LOMA (Fig. S3a-b), there is residual distance change (1.3 mm/yr for P215 or 1.25 mm/yr for SODB) after removing secular motion, which is similar with pre-

Morgan Hill residual (~1.5 mm/yr). For HAML – AMER (Fig. S3c), the secular motion-free residual is ~1 mm/yr after 2010 and is the same as pre-Morgan Hill event (1 mm/yr). For LOMA – AMER (Fig. S3d-f), there is ~1.6 mm/yr residual for LP1X or SODB substitute between 2005-2010, and < 1 mm/yr for P215. However, there is a change of rate of SODB in 2011 and changed the time series significantly in Figs S3b and e.

The secular motion-free distance changes of pairs MHCB – LUTZ (Fig. S3c), LP1X – LUTZ (Fig. S3d), and P215 – LUTZ (Fig. S3f) are less than 1 mm/yr before the Loma Prieta earthquake and after 2010. For MHCB – P215 (Fig. S3a) and LP1X – LUTZ (Fig. S3d), the secular motion-free distance changes are > 1.2 mm/yr. For station SODB, there is a change of rate in 2011 so it is difficult to include data after 2011. However, MHCB – SODB and SOBD – LUTZ show similar pattern and rate as MHCB – P215 and P215 – LUTZ, respectively. As a result, the Morgan Hill event only affects the pair HAML – LOMA, but it is still hard to quantify the slip rate readjustment of the Calaveras fault near Morgan Hill until more years of GPS time series data are collected.

S2. Deformation in the Santa Clara Valley

In the eastern Santa Clara Valley (Figs S4 & S5a), there is a change in velocity across the Silver Creek fault indicating deformation due to groundwater level changes [*Schmidt and Bürgmann*, 2003]. Near Palo Alto, there is a ~2 mm/yr uplift during 1992 – 2000 and nearly 0 mm/yr afterward. In part of the Santa Clara Valley, we see significant seasonal uplift/subsidence throughout the time series (Fig. S5b), but this effect subsides after 2006. We use sine and cosine functions with a one-year period to fit the seasonal uplift/subsidence in the entire time series by using the least squares method (see

Supplementary Information S3). Fig. S5a shows the result of seasonal amplitude based on this method, and we mark the regions that have seasonal change greater than 1cm in Fig. 3. There is a stronger seasonal amplitude in the northern Santa Clara Valley throughout the entire period with the peak amplitude of ~2 cm (dashed line in Fig. 3), which agrees with a recent study by *Chaussard et al.* [2014]. The time series of a point in this region shows high correlation between annual precipitation and surface deformations (Fig. S5b). This region (dashed line in Fig. 3) roughly coincides with the observed land subsidence from 1934 to 1960 (Poland and Ireland, 1988; Schmidt and Bürgmann, 2003; Chaussard et al., 2014). We assume that this seasonal surface deformation is not related to tectonic movement, and hence, exclude this region from postseismic modeling.

S3. Seasonal change in InSAR time series

In the InSAR time series, the seasonal change in time series can be described as,

$$a_{x,y} \times sin(2\pi t) + b_{x,y} \times cos(2\pi t), \quad [S1]$$

where a and b are constants that describe the coefficients of the sine/cosines functions and (x,y) is the location of a given pixel. The amplitude of the seasonal effect is $(a^2 + b^2)^{0.5}$, and the phase shift (i.e. when is the peak of seasonal effect) is $2\pi \times \tan^{-1}(a/b)$. In this study, we fit the InSAR time series with a combination of a linear mean velocity and the seasonal terms with least square inversions. In other word, the time series can be described as,

$$y_{x,y}(t) = \Delta v_{x,y} \times t + a_{x,y} \times sin(2\pi t) + b_{x,y} \times cos(2\pi t) + \varepsilon_{x,y}(t), \quad [S2]$$

where $\Delta v_{x,y}$ is the annual mean velocity. Eq. S2 can be rewritten as

$$\mathbf{d} = \mathbf{G}\ \mathbf{m} + \boldsymbol{\varepsilon}, \quad [S3]$$

where

$$\mathbf{d} = \begin{bmatrix} y_{x,y}(t_1) \\ y_{x,y}(t_2) \\ \dots \\ y_{x,y}(t_N) \end{bmatrix}, \mathbf{G} = \begin{bmatrix} sin(2\pi t_1) & cos(2\pi t_1) & t_1 & 1 \\ sin(2\pi t_2) & cos(2\pi t_2) & t_2 & 1 \\ \dots & \dots & \dots & \dots \\ sin(2\pi t_N) & cos(2\pi t_N) & t_N & 1 \end{bmatrix}, \mathbf{m} = \begin{bmatrix} a_{x,y} \\ b_{x,y} \\ \Delta v_{x,y} \\ k_{x,y} \end{bmatrix}, \qquad [S4]$$

and here $k_{x,y}$ is the model residual. The estimated model ($\mathbf{m}^{\mathbf{est}}$) of Δv, a, and b based on least squares is:

$$\mathbf{m}^{\mathbf{est}}(\Delta v,a,b) = (\mathbf{G}^{\mathrm{T}}\,\mathbf{G})^{-1}\,\mathbf{G}^{\mathrm{T}}\,\mathbf{d}. \qquad [S5]$$

S4. InSAR uncertainty analysis

To account for spatial correlation due to atmospheric noise in every acquisition, we follow the approach by *Sudhaus and Jónsson* [2009] and *Liu et al.* [2011]. In this approach we first estimate sample covariogram of an approximately 25 × 25 km^2 area in each SAR phase residual map This area is east of the Calaveras fault where no significant crustal deformation is observed, and is highlighted in a black box in Fig. S4. Here residual means the remaining phase values that cannot be modeled by linear and seasonal deformation terms ($\varepsilon_{x,y}$(t) term in Eq. S2 in Supplementary Information S3). The covariogram is defined as,

$$\hat{C}(h_c) = \frac{1}{2N}\sum_{i=1}^{N} d(\mathbf{r}_i)\cdot d(\mathbf{s}_i), \qquad [1]$$

where N is the number of scatterer pairs $d(\mathbf{r}_i)$ & $d(\mathbf{s}_i)$ that has distance h_c in the area. We evaluate the covariance as a function of distance h_c in 500 m intervals from 0 to 20 km. As shown in the figure below, we see higher covariance when pixels are close to each other. We can also observe that the covariance drop to near zero beyond 3-9 km distance in all acquisitions.

After computing the covariograms, we model the covariogram structure with the equation suggested by *Liu et al.* [2011],

$$\sigma^2 e^{-h/L} \cos(h/L), \qquad [2]$$

where h is the distance between pixels, σ^2 is the peak covariance when $h = 0$, and L is the characteristic distance of the modeled covariogram. σ^2 and L are the two parameters we can estimate for all SAR acquisitions using least squares. The modeled covariogram is shown with black lines in Fig. S12 and the distribution of σ^2 and L computed from all SAR acquisitions is shown in Fig. S13.

After this calculation we can generate the variance-covariance matrix ($\mathbf{Q}_i$) of each acquisition by using the estimated σ^2 and L values for the distance between scatterer pairs. The variance-covariance matrix is then a $M \times M$ matrix, where M is the number of the scatterers used for viscoelastic relaxation modeling.

Reference:

Liu Z., Dong, D., and Lundgren, P. (2011), Constraints on time-dependent volcanic source models at Long Valley Caldera from 1996 to 2009 using InSAR and geodetic measurements, *Geophys. J. Int.*, *187*, 1283-1300, doi:10.1111/j.1365-246X.2011.05214.x

Sudhaus, H., and Jónsson, S., (2009), Improved source modeling through combined use of InSAR and GPS under consideration of correlated data errors: application to the June 2000 Kleifarvatn earthquake, Iceland, *Geophys. J. Int.*, *176*, 389-404, doi:10.1111/j.1365-246X.2008.03989.x

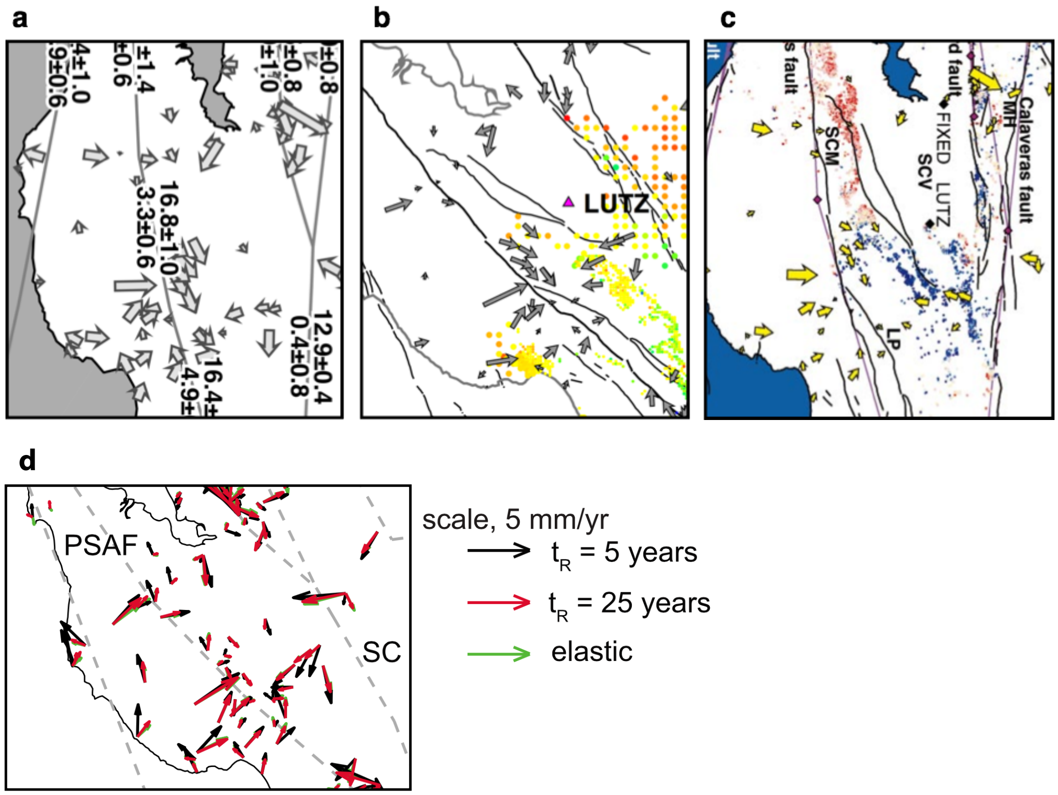

Figure S1. Residuals from interseismic models in (a) block model of d'Alessio et al. [2005], (b) deep dislocation model of Johanson & Bürgmann [2005], (c) deep dislocation model of Bürgmann et al. [2006], (d) residual of joint afterslip and viscoelastic relaxation model by Johnson & Fukuda [2010].

a

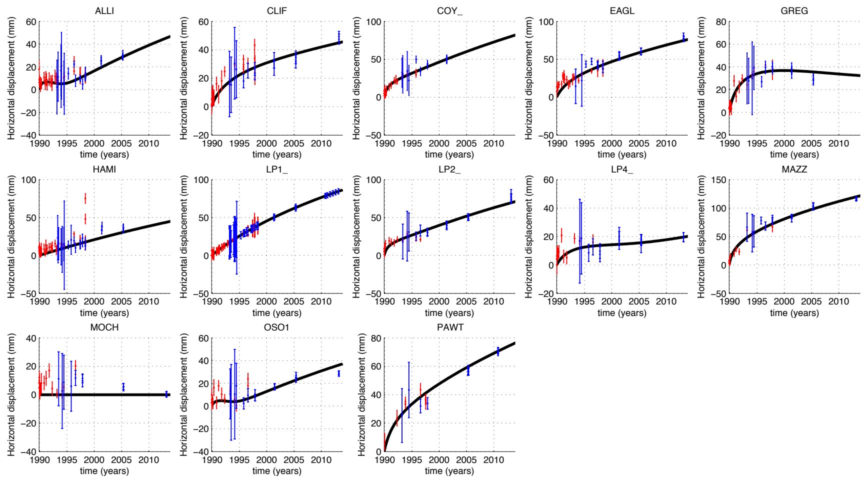

b

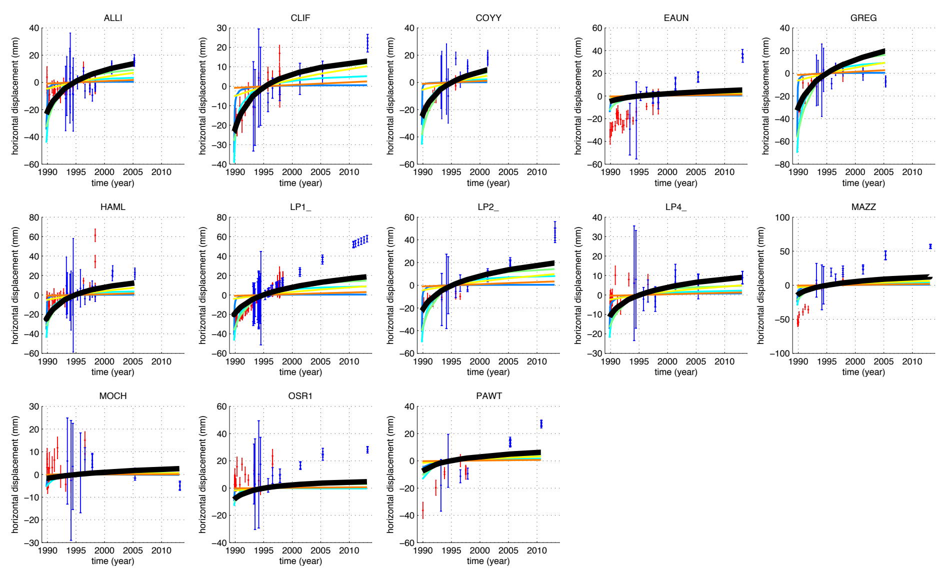

Figure S2. (a) GPS time series between 1989.8 and 2013 with interseismic velocities estimated from preseismic trilateration measurements [*Bürgmann*, 1997] subtracted. The time series of each station is relative to MOCH, east of the Calaveras fault. The red and blue points are data from *Segall et al.* [2000] and *USGS* (2014), respectively. The black curves are fitted postseismic displacements assuming logarithmic functions (see Section

3.2). **(b)** Viscoelastic relaxation models fittings to GPS stations in horizontal time series. The colored lines represent different viscoelastic model (the same color-code as Fig. 4).

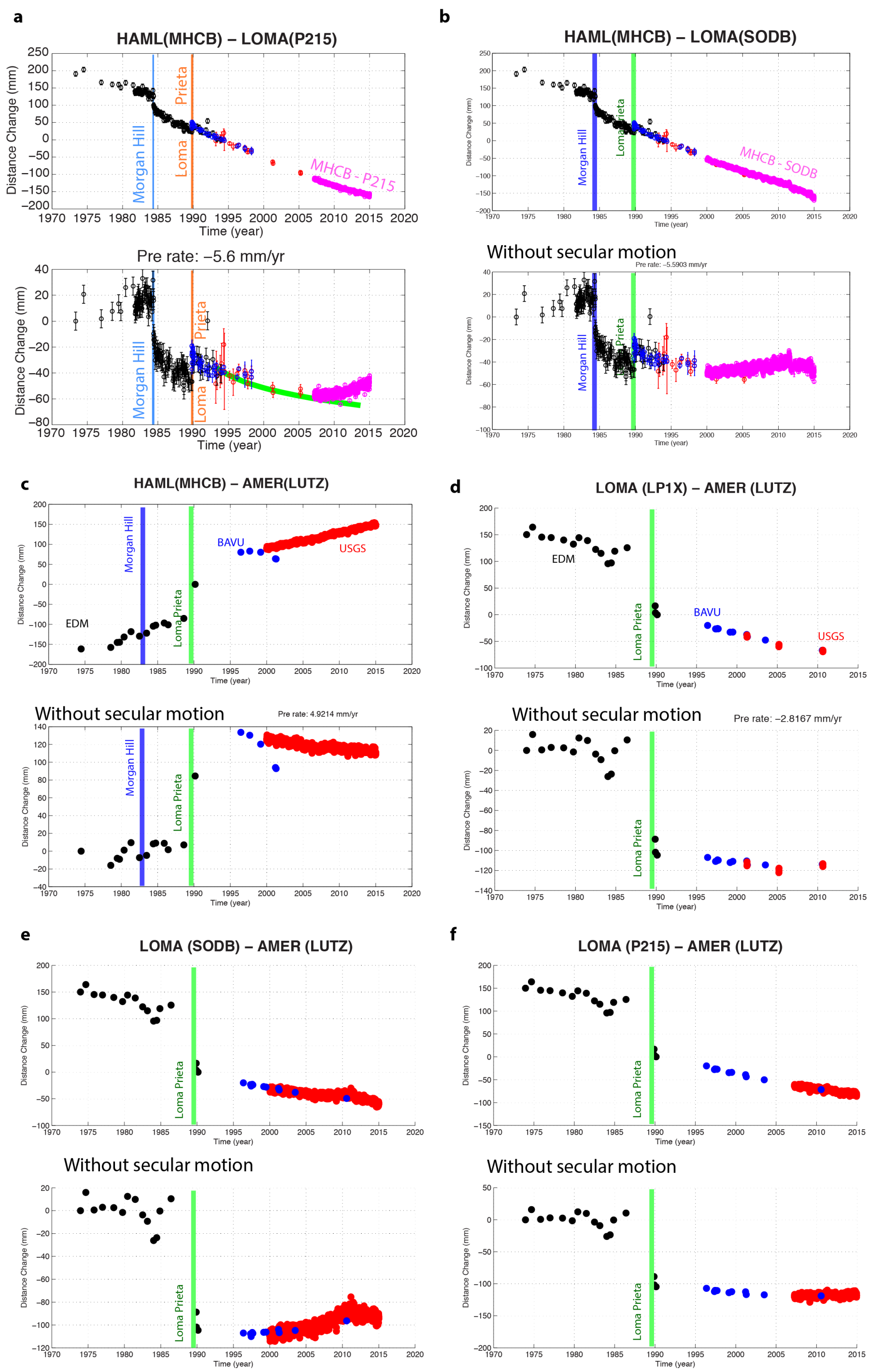

Figure S3. Shortening rate between pairs **(a)** HAML (MHCB) – LOMA (LP1X), **(b)** HAML (MHCB) – LOMA (SODB), **(c)** HAML (MHCB) – AMER (LUTZ), **(d)** LOMA (LP1X) – AMER (LUTZ), **(e)** LOMA (SODB) – AMER (LUTZ), and **(f)** LOMA (P215)

– AMER (LUTZ). The station names inside parentheses represent stations nearby the original EDM benchmarks, which are considered as extended distance change time series. In all sub-figures, the top rows show the original time series and the bottom rows show the Loma Prieta postseismic time series.

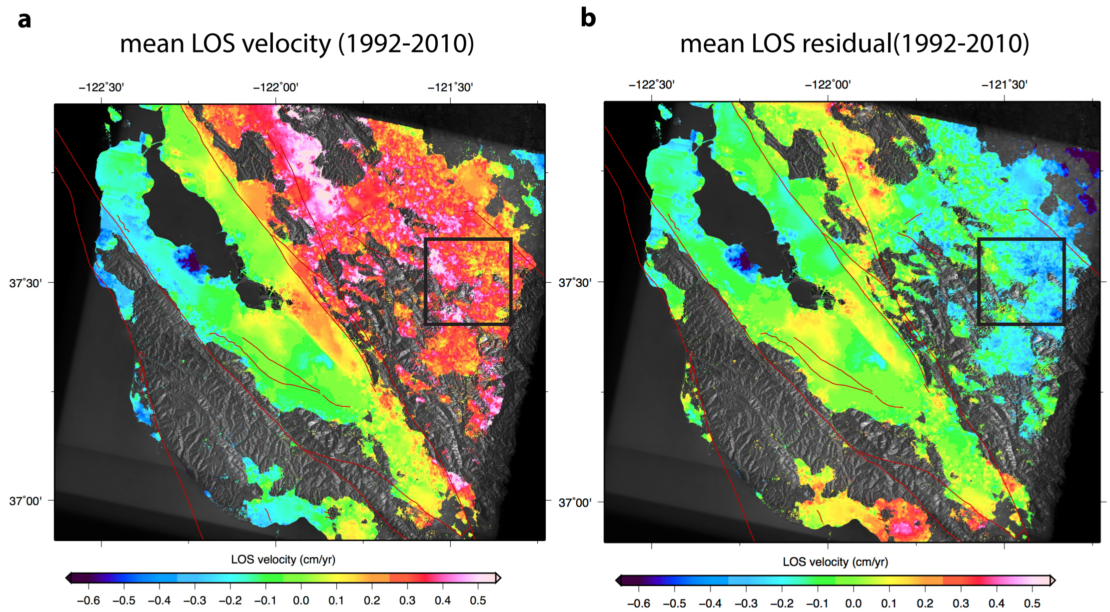

Figure S4. (a) Mean line of sight (LOS) velocity during 1992 – 2010. **(b)** Mean LOS velocity residual (without secular motion). The black box in each sub-figure indicates the area where the InSAR covariogram is computed for InSAR uncertainty analysis (see Supplementary Information S4).

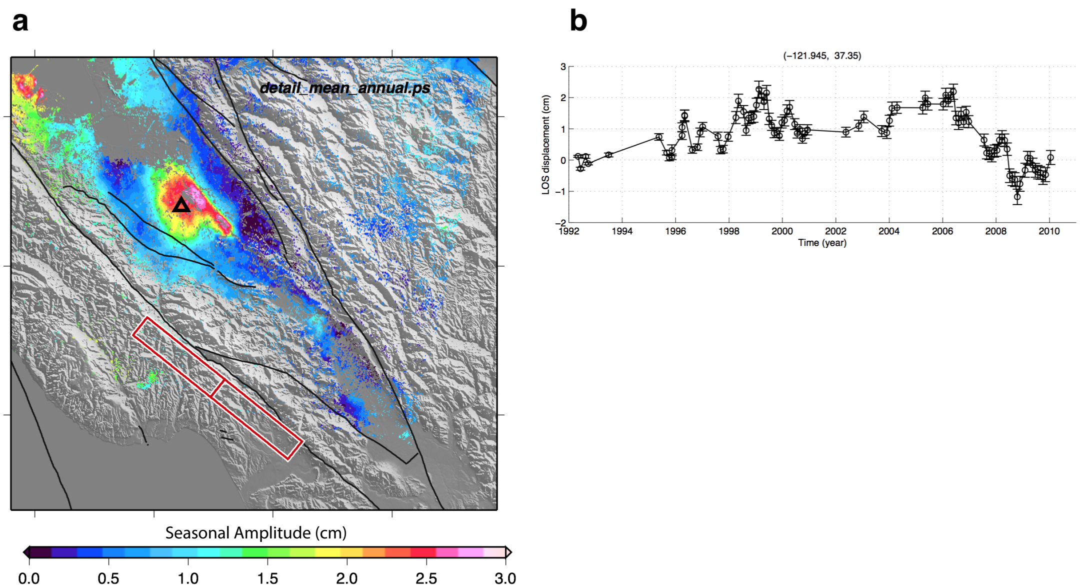

Figure S5. (a) Amplitude of seasonal LOS deformation. **(b)** Time series of a point (the yellow triangle) in North Santa Clara valley.

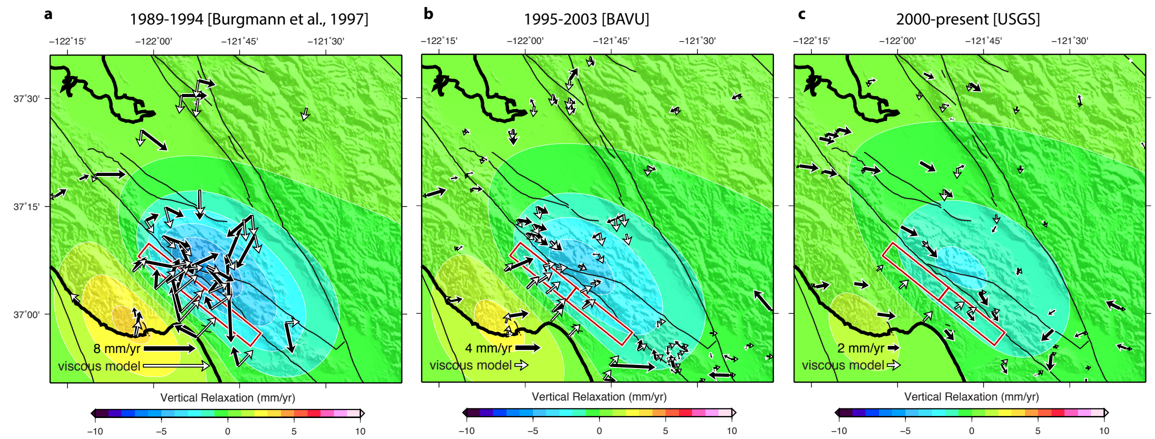

Figure S6. Viscoelastic relaxation prediction to GPS stations in **(a)** *Bürgmann et al.* [1997], **(b)** *Johanson and Bürgmann* [2005], and **(c)** USGS PBO stations.

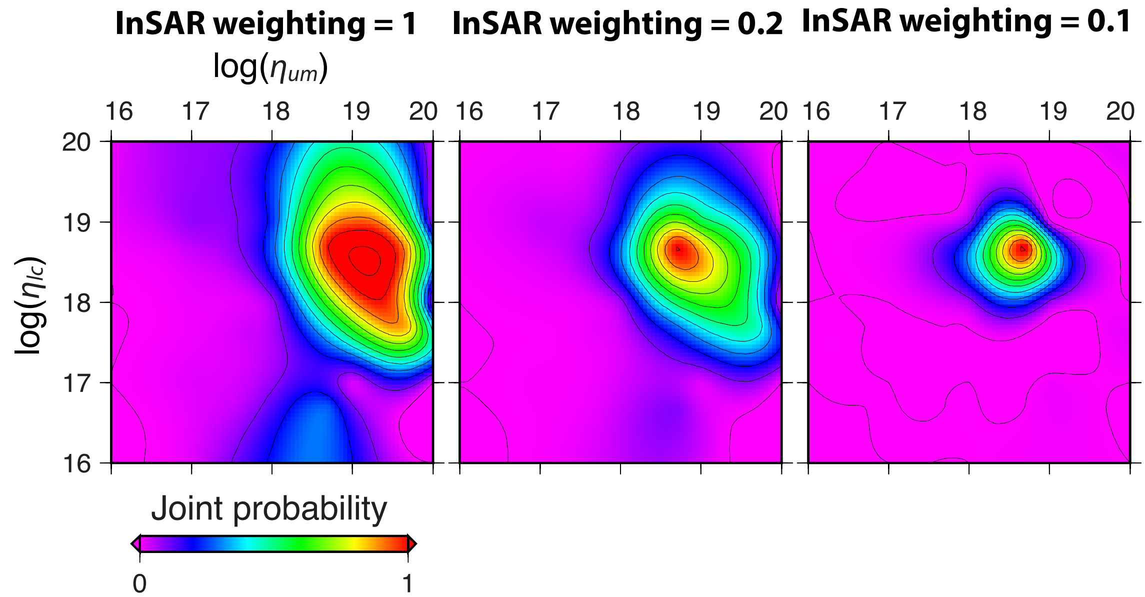

Figure S7. Joint inversion with different GPS weighting from one (left) to ten (right). The inferred upper mantle viscosity varies from 1.3×10^{19} to 4×10^{18} Pa s when increases GPS weighting, whereas the lower-crustal viscosity remains the same.

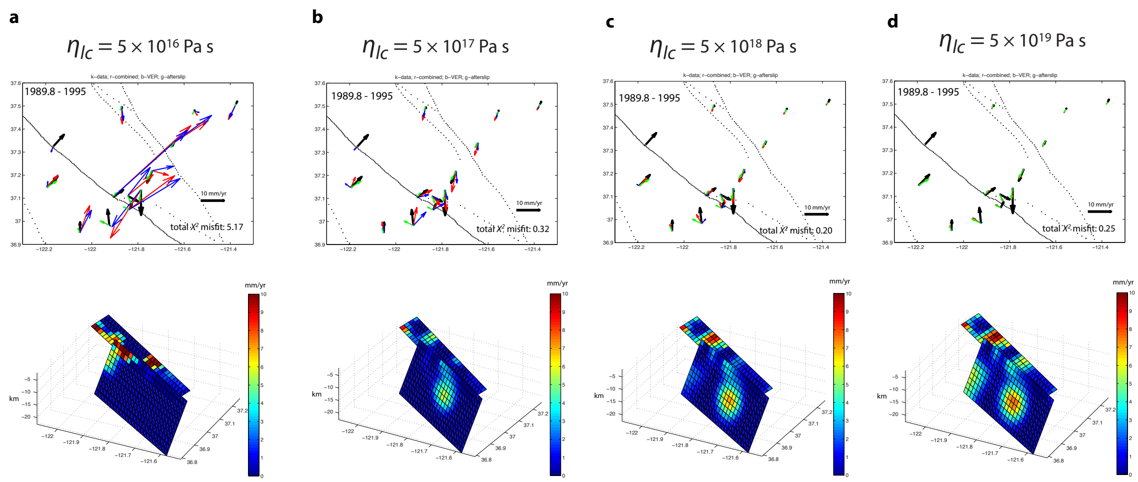

Figure S8. Afterslip fitting to 1989-1995 GPS time series when the lower-crustal viscositiy is **(a)** 5×10^{16} Pa s, **(b)** 5×10^{17} Pa s, **(c)** 5×10^{18} Pa s, and **(d)** 5×10^{19} Pa s. the VE prediction (blue arrows) include contribution from upper mantle with viscosity fixed at 2×10^{19} Pa s and the lower crust with varying viscosity. For the higher-viscosity realizations, the contribution of the relaxation is quite modest. The top row shows viscoelastic relaxation – afterslip combined model fitting to GPS time series (black-GPS; blue-viscoelastic relaxation; green-afterslip; red-combined model). The chi-square misfit is shown in the lower right of each plot. The bottom row shows afterslip distribution. Note the lower-crustal viscosity = 5×10^{18} Pa s model can best describe the 1989 - 1995 GPS time series.

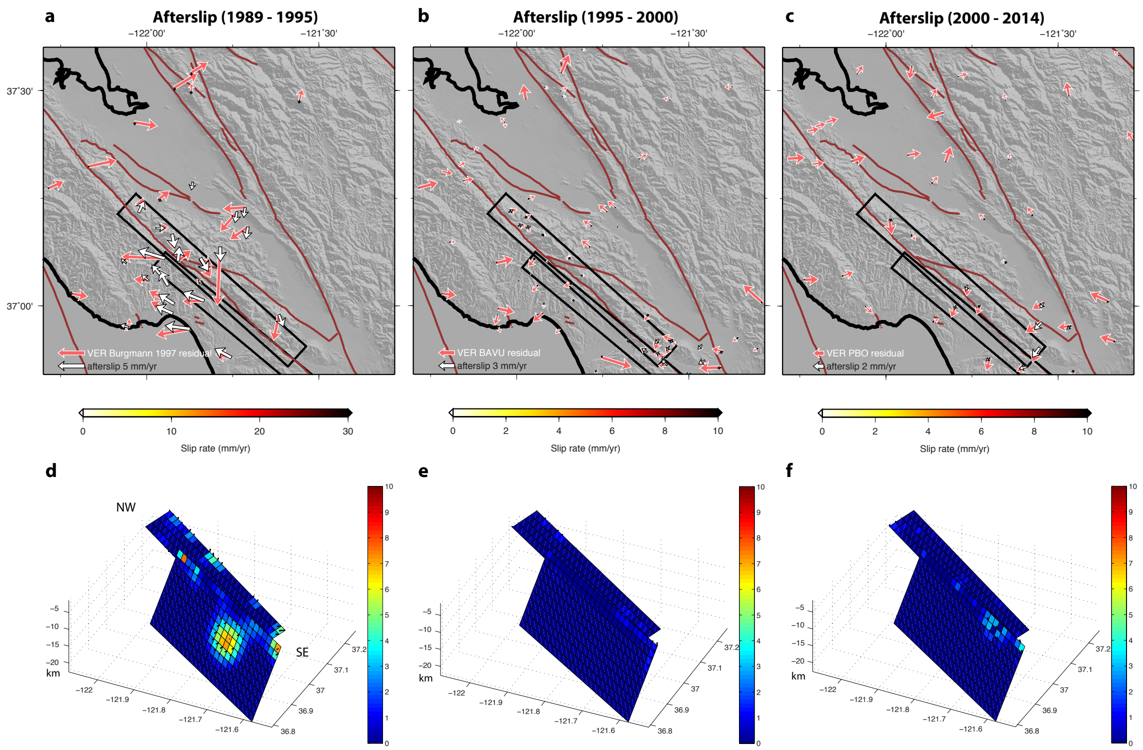

Figure S9. Afterslip distribution (color contoured planes) in **(a)** 1989 – 1995, **(b)** 1995 – 2000, and **(c)** 2000 onward time periods. The black arrows are viscoelastic model misfits (residuals in **Fig. 6**) and white arrows are surface displacements due to afterslips on the two faults. The fault geometries are based on *Bürgmann et al.* [1997]. **(d-f)** Afterslip distribution on each fault plane. The orientation of the arrows indicate rake.

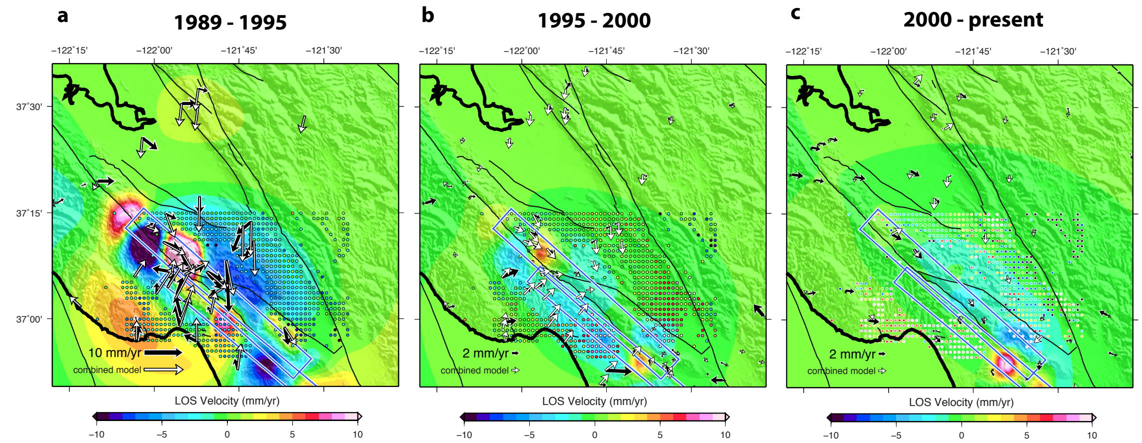

Figure S10. Viscoelastic relaxation and afterslip combined model in **(a)** 1989 – 1995 (data: *Bürgmann et al*., 1997), **(b)** 1995 – 2000 (data: *Johanson and Bürgmann*, 2005), and **(c)** 2000-present (*USGS*, 2014) time periods. The black arrows are GPS postseismic displacements in different, and the white arrows are the multiple-mechanism models in each time periods. The background colors show the predicted surface relaxation prediction in LOS.

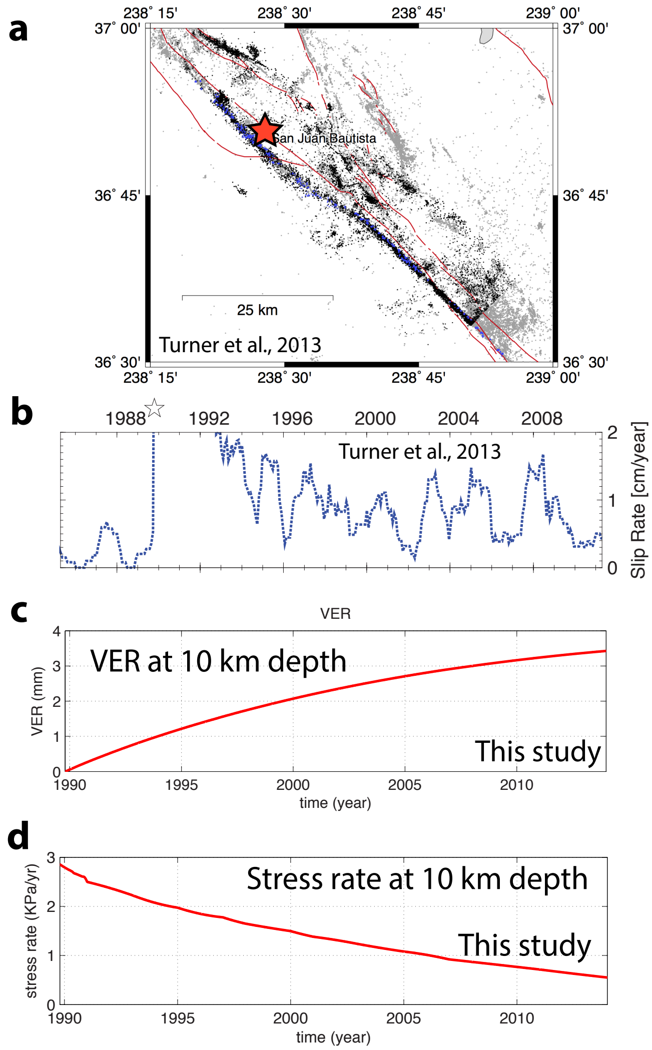

Figure S11. (a) Map of repeaters SE of the Loma Prieta earthquake (After *Turner et al.*, 2013). The blue circles are the repeaters along the San Andreas fault, and the red circles are repeaters along Sargent fault. The red star indicates the location we estimate viscoelastic relaxation (VER). (b) Slip rate along the San Andreas fault calculated from the repeaters (blue dashed line). (c) Predicted VER at the red start in (a) at 10 km depth. (d) Predicted stress rate due to VER of the same location as (c).

Time: 1996.24 Time: 1996.33 Time: 2002.38

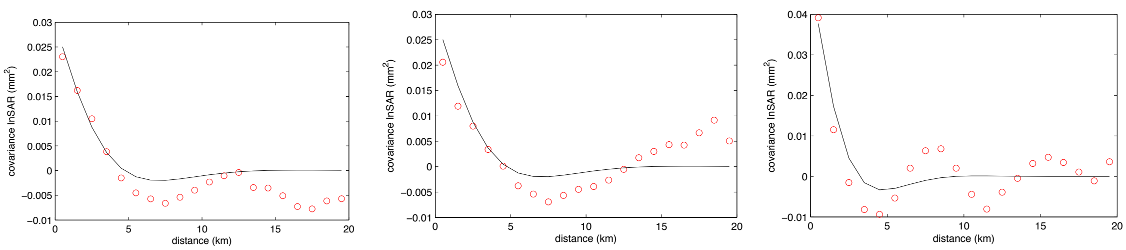

Figure S12. Three examples of covariogram of selected acquisitions. The red dots are the observed covariance along data-point pair distances from 0 to 20 km with a 500 m interval. The black lines are the modeled covariogram using Eq. 2.

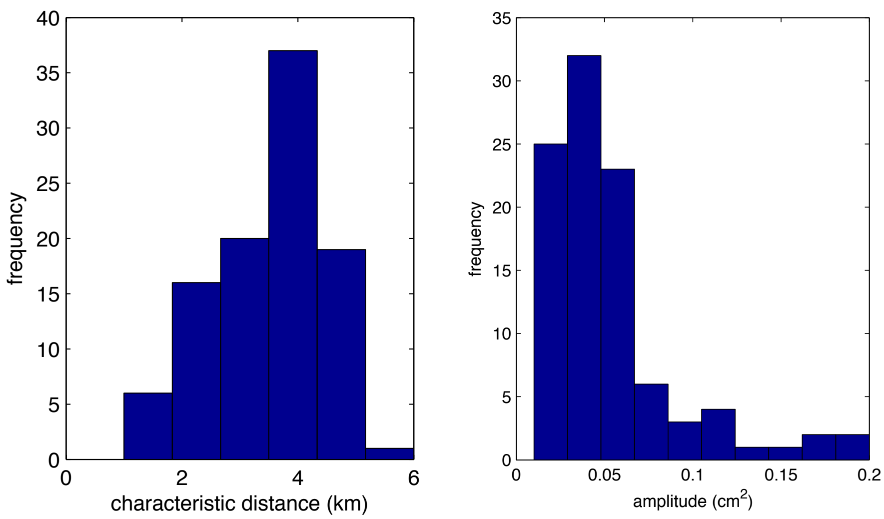

Figure S13. Histograms of the modeled σ^2 and L in in Eq. 2. Note most of the characteristic decay length (L) is ~4 km and the characteristic amplitude is ~0.04 cm^2 in our study area.

Table S1. ERS-1/2 acquisitions (track: 70; frame: 2853) used in this study.

yymmdd	yymmdd	yymmdd
19920610	19980926	20011229
19920715	19981031	20020202
19920819	19981205	20020518
19920923	19990109	20020622
19930106	19990213	20020727
19950519	19990320	20021005
19950901	19990424	20021109
19951007	19990529	20021214
19951110	19990703	20030118
19951111	19990807	20040103
19951215	19990911	20051203
19960329	19991016	20060107
19960330	19991120	20060211
19960504	19991225	20060318
19960817	20000129	20060701
19961026	20000304	20060805
19961130	20000408	20060909
19970104	20000617	20061014
19970802	20000722	20061118
19970906	20000826	20061223
19971011	20000930	20070127
19971220	20001104	20071103
19980404	20001209	20071208
19980509	20010915	20080531
19980718	20011020	20080705
19980822	20011124	20080809

Table S2. Envisat acquisitions (track: 70; frame: 2853) used in this study.

yymmdd	yymmdd
20030118	20071208
20030503	20080112
20030920	20080216
20031129	20080322
20040103	20080426
20040207	20080531
20040417	20080705
20050402	20080809
20050507	20080913
20050611	20081018
20060211	20081122
20060318	20090131
20060422	20090307
20060527	20090411
20060701	20090516
20060805	20090620
20061014	20090725
20061118	20090829
20061223	20091003
20070721	20091107
20070825	20091212
20070929	20100116
20071103	20100220